

Chemodynamics of outer halo dwarf stars, including potential *Gaia*-Enceladus and *Gaia*-Sequoia members

Stephanie Monty,^{1,2}★ Kim. A. Venn¹, James M. M. Lane,^{1,3} Deborah Lokhorst,^{1,3} David Yong²

¹*Department of Physics and Astronomy, University of Victoria, Victoria, BC V8W 3P2, Canada*

²*Research School of Astronomy and Astrophysics, Australian National University, Canberra, ACT 2611, Australia*

³*Department of Astronomy and Astrophysics, University of Toronto, 50 St. George Street, Toronto, ON M5S 3H4, Canada*

Accepted XXX. Received YYY; in original form ZZZ

ABSTRACT

High resolution Keck HIRES and Gemini GRACES spectra are combined with Gaia DR2 photometry and astrometry to re-examine the low-metallicity, kinematically interesting dwarf stars studied by Stephens & Boesgaard (2002). These stars, spanning a metallicity range of $-1.5 > [\text{Fe}/\text{H}] > -3$, were originally selected as outer halo dwarf stars because of their large apocentric radii, large distances from the Milky Way plane and/or highly elliptical or retrograde orbits. Using additional chemical and kinematic criteria, we select a subsample of six stars (test cases) to redetermine stellar parameters and abundances using new model atmospheres and updated atomic data. We confirm two of the six stars in our sample to be very metal-poor, with $[\text{Fe}/\text{H}] \sim -2.3$ (G158-100, G037-037) and find two other stars to be Mg-poor at intermediate metallicities $[\text{Fe}/\text{H}] \sim -1.5$ (G184-007 and G189-050). The latter signature is suggestive of origins in an accreted dwarf galaxy. Gaia DR2 data is used to redetermine the orbital parameters for the entire SB02 sample. We find nine stars to be dynamically coincident with the *Gaia*-Enceladus satellite merger, including one very low metallicity star (G238-030) ($[\text{Fe}/\text{H}] \sim -3.6$). Another 17 stars are found to be dynamically coincident with the *Gaia*-Sequoia accretion event, including one very metal-poor star near $[\text{Fe}/\text{H}] = -3.5$. Both metal-poor stars have low masses and isochrone ages older than 10 Gyr. A knee in $[\alpha/\text{Fe}]$ is found in the *Gaia*-Enceladus associated stars, near $[\text{Fe}/\text{H}] \sim -1.6$, while the location of an $[\alpha/\text{Fe}]$ is less clear in the *Gaia*-Sequoia sample. If the metal-poor stars in these samples are true members of the *Gaia*-Enceladus and *Gaia*-Sequoia remnants, they present unique opportunities to probe the low metallicity tail and early star formation history of these systems.

Key words: Galaxy: halo – Galaxy: stellar content – Galaxy: chemical evolution – Local Group – stellar abundances

1 INTRODUCTION

Our view of the stars in the solar neighbourhood has drastically changed in the past year with the second data release (DR2) of the European Space Agency’s Gaia mission (Gaia Collaboration et al. 2016, 2018). The superb astrometric parameters, radial velocities, and photometric data of the billion-star-dataset have impacted fundamental stellar parameter determinations, yielded the first detailed orbits of nearby stars, and revealed a wide variety of structures and streams not previously identified in our Galaxy.

One of the most interesting *Gaia* results thus far has been the discovery of two parallel colour sequences in the Gaia HR diagram of stars in the solar neighbourhood. Although they are currently found within 2.5 kpc of the solar neighborhood, these stars have high total or tangential velocities indicating that they belong to the Milky Way (MW) halo. Both Helmi et al. (2018) and Haywood et al. (2018) have cross matched the dual sequence stars with the SDSS APOGEE database (Majewski et al. 2017) and the Nissen & Schuster (2010) high orbital energy stars, to find that one of the sequences (their “blue sequence”) is dominated by stars with lower $[\alpha/\text{Fe}]$ ratios. Furthermore, a subset of the stars on the blue sequence are highly retrograde ($V < -500$

★ E-mail: Stephanie.Monty@anu.edu.au

kms⁻¹) and found in a flattened disk. Both papers then suggest that the blue sequence is dominated by stars from an accreted satellite galaxy with a unique star formation history and chemical evolution (or possibly multiple satellite mergers).

The idea that accreted stars dominate the low $[\alpha/\text{Fe}]$ sequence was also proposed by (Nissen & Schuster 2010, 2011, NS10/11), using a smaller sample of stars, and by Belokurov et al. (2018a) using the distribution of many of RR Lyrae stars in period-amplitude space. Both Belokurov et al. (2018b) and Helmi et al. (2018) have proposed a single merger event, the “*Gaia Sausage*” or “*Gaia-Enceladas*” merger¹, ~10 Gyr ago to explain the formation of the MW inner halo. This is also consistent with the findings of Haywood et al. (2018) who show that the blue sequence stars are slightly younger than red sequence stars based on ages derived using Dartmouth Stellar Evolution Database (DSED) isochrones (Dotter et al. 2008). Alternatively, Myeong et al. (2019) propose two merger events, one to explain the moderately eccentric, strongly retrograde stars and the other to explain the weakly prograde, highly eccentric stars. The progenitors of these two events are referred to as *Gaia-Sequoia* and the “*Gaia Sausage*” (*Gaia-Enceladas*) respectively. Helmi et al. (2018) and Haywood et al. (2018) also suggest that the red sequence is consistent with the Galactic thick disk stars, and that the velocity distribution could be consistent with a dynamical heating of the precursor to the thick disk by the merger. This had been proposed earlier by several authors (e.g., Gilmore & Wyse 1985; Navarro et al. 2011) in earlier studies of the chemo-dynamical trends with height from the MW disk.

Stars in the solar neighbourhood with distinctly different chemical abundances in high energy orbits have been known for nearly two decades (e.g., Fulbright 2002; Stephens & Boesgaard 2002; Venn et al. 2004; Nissen & Schuster 2010; Hawkins et al. 2015; Battaglia et al. 2017). The overwhelming majority of stars with halo kinematics have high $[\alpha/\text{Fe}] \sim +0.4$, suggesting that they formed in regions with a high star formation rates such that only massive stars and Type II SNe contributed to their chemical enrichment. Stars with lower $[\alpha/\text{Fe}] \leq 0.2$ dex tend to be metal-poor stars, $-1.5 \leq [\text{Fe}/\text{H}] \leq -0.5$, with a slightly declining trend in $[\alpha/\text{Fe}]$ with $[\text{Fe}/\text{H}]$. This chemical pattern is thought to be the result of slower chemical evolution, with chemical enrichment coming primarily from type Ia supernovae and/or the result of fewer high mass stars in the region (a truncated upper initial mass function (IMF)), (e.g., Tolstoy et al. 2003; McWilliam et al. 2013).

Importantly, the high- α and low- α sequences are also traced in a number of other elements (Cu, Zn, Y, Ba, Na, Al, Ni; Nissen & Schuster 2011; Hawkins et al. 2015). The lower abundances of these additional elements has been attributed to larger contributions from metal-poor asymptotic giant branch (AGB) stars, consistent with slower star formation and chemical evolution. In their two studies, Fernández-Alvar et al. (2015, 2017) examined trends in Ca, Mg, and Fe in MW halo stars as a function of galactocentric distance using SDSS DR10 (Ahn et al. 2014) (out to $R \sim 80$ kpc) and APOGEE DR12 data (Majewski et al. 2017) (out to $R \sim 30$

kpc.) Overall, they found the median $[\alpha/\text{Fe}]$ abundance was lower by a modest ≥ 0.1 dex for halo stars with $[\text{Fe}/\text{H}] \sim -1.1$ at distances of $R_{\text{GC}} \geq 15$ kpc, confirming that lower α stars are found at large galactocentric distances.

Independent of global trends in the MW halo, a few metal-poor stars with very distinctive chemical abundances have also been found. In their study, Battaglia et al. (2017) derive chemical abundances from high resolution optical spectroscopy of 28 red giant stars in the outer halo ($R_{\text{apo}} > 15$ kpc from the galactic centre and height $Z_{\text{max}} > 9$ kpc from the MW mid-plane) to examine the halo’s chemical diversity. They find that while the metallicity of the stars in their sample ranges from $-3.1 < [\text{Fe}/\text{H}] < -0.6$, the $[\alpha/\text{Fe}]$ abundances remain high across all metallicities, similar to stars in the solar neighbourhood (with the exception of one star anomalously low $[(\text{Ca}, \text{Mg})/\text{Fe}] \leq -0.2$ that is associated with the Sagittarius stream). Although they do not find the $[\alpha/\text{Fe}]$ signature of accretion, they interpret the high values of $[\text{Ba}/\text{Fe}]$ and $[\text{Ba}/\text{Y}]$ they find in the intermediate metallicity range stars in their sample ($[\text{Fe}/\text{H}] \sim -1.5$), as evidence for accretion in the outer halo. The high values they find are relative to inner halo stars of the same metallicity and indicate pollution from metal-poor AGB stars. Only one of the stars in their study has measurements in the APOGEE database, but it shows good agreement for elements in common.

In an earlier study, Ivans et al. (2003) found three distinct metal-poor dwarf/sub-giant halo stars with $[\text{Fe}/\text{H}] \sim -2$ and low $[\alpha/\text{Fe}]$ using high resolution optical spectroscopic data. They showed that each star has additional unique chemical characteristics, such as enhancements in iron-group elements, with one star in their study, CS 22966-043 showing an enormous abundance of $[\text{Ga}/\text{Fe}] = +1.75$ (LTE). They suggest that these chemically peculiar stars could have formed in regions enhanced in SN Ia products, similar to the interpretations of the chemical peculiarities of stars in the Carina and Sextans dwarf galaxies (Venn et al. 2012; Jablonka et al. 2015; Norris et al. 2017). Clearly our picture of the MW halo is complex, both chemically and kinematically.

Upon examining outer halo stars in the literature, we noticed that a sample of outer halo *dwarf* stars studied by (Stephens & Boesgaard 2002, SB02) had not been revisited. The SB02 sample is interesting because the sample includes stars more metal-poor ($-3 < [\text{Fe}/\text{H}] < -1.5$) than the sample of NS10/11 with large apocentric radii ($R_{\text{apo}} > 15$ kpc) and slightly lower $[\alpha/\text{Fe}] \sim 0.1 - 0.2$ dex than the majority of halo stars of similar metallicities. In the original study, SB02 conclude that the stars in their sample do not carry the chemical signatures of an accreted population, thereby forming in localized star forming regions in situ² the MW halo and birthed into orbits reflecting early halo kinematics. Coupling information from the Gaia DR2 data release with significant improvements in stellar spectral analyses, we revisit the chemo-dynamic analysis of the SB02 stars.

The paper is organised with some discussion of the results throughout. In Section 2 we introduce a subset of the SB02 data re-analysed in this work, briefly describing

¹ Hereafter, we refer to this system only as *Gaia-Enceladas*.

² In this work, “in situ” refers to stars that formed within the Milky Way.

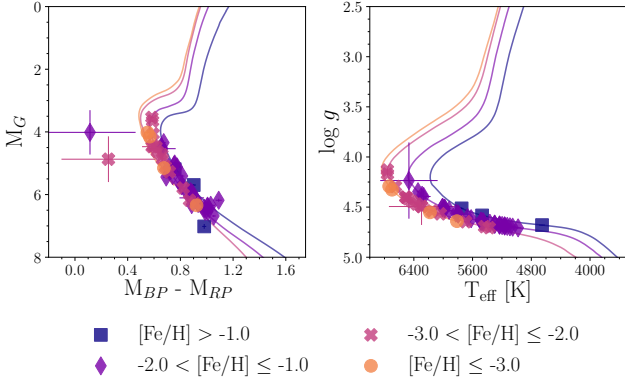


Figure 1. The isochrone mapping method for the entire Gaia-SB02 sample. See Section 2.1 for details on the isochrone parameters and sample divisions.

the techniques used to re-determine stellar parameters, and comparing to the original SB02 parameters. In Section 3 our updated stellar abundances are discussed in the context of both the original SB02 study and the study of NS10/11. In Section 4 the orbital parameters are updated using Gaia DR2 data, and we discuss the potential origins of the stars in the SB02 sample and accretion history of the Galaxy, highlighting the combination of the chemical and dynamical results. Section 5 summarises the key results of the paper.

2 THE SB02 TARGETS

Stephens & Boesgaard (2002) selected their original sample from the Carney et al. (1994) catalogue of high proper motion stars. The Carney et al. (1994) catalogue was compiled over many years using photometry and radial velocities for almost 500 stars from the Lowell Proper Motion Catalog along with estimates of stellar distances. Orbital parameters including, apocentric radii (R_{apo}) and maximum height from the disc (Z_{max}), were determined in the catalogue using the two component MW model of (Bahcall et al. 1983).

SB02 selected 56 dwarf stars that satisfy one of three orbital criterion:

- Outer halo ($R_{\text{apo}} > 16$ kpc),
- High halo ($Z_{\text{max}} > 5$ kpc), or
- Extreme retrograde orbit ($V < -400$ km/s).

In the following section we discuss our re-analysis of the SB02 data, including a subset of chemically and kinematically distinct stars. We do not include a detailed discussion of the technique we use to re-derive stellar parameters and instead direct the reader to the Appendix (A1)

2.1 SB02 in the Era of Gaia

Stellar parameters are determined for 55/56 stars in the SB02 sample using Gaia DR2 G vs $BP - RP$ colour-magnitude values of each star in an isochrone-mapping technique described in Section A1. One star in the SB02 was cut from our analysis as it was not available in Gaia DR2

Table 1. Average differences in effective temperature and surface gravity between this study (“MV19”) and that of SB02 for each metallicity bin.

Bin	ΔT_{eff} [K] (MV19-SB02)	$\Delta \log g$ [dex] (MV19-SB02)
$[\text{Fe}/\text{H}] > -1.0$	$+54.6 \pm 37.5$	0.06 ± 0.01
$-2.0 < [\text{Fe}/\text{H}] \leq -1.0$	$+179 \pm 119$	0.15 ± 0.17
$-3.0 < [\text{Fe}/\text{H}] \leq -2.0$	$+440 \pm 104$	0.47 ± 0.15
$[\text{Fe}/\text{H}] \leq -3.0$	$+699 \pm 147$	0.77 ± 0.29

archive³. Errors associated with the final stellar parameters are determined using a Monte-Carlo approach to explore the photometric and parallactic parameter uncertainties. Prior to constructing colour-magnitude diagrams (CMDs), we split the SB02 sample into smaller subsamples using the same metallicity bins as those used in SB02. The bins are as follows:

- i) $[\text{Fe}/\text{H}] > -1.0$, $[\alpha/\text{Fe}] = 0$,
- ii) $-2.0 < [\text{Fe}/\text{H}] \leq -1.0$, $[\alpha/\text{Fe}] = 0.2$,
- iii) $-3.0 < [\text{Fe}/\text{H}] \leq -2.0$, $[\alpha/\text{Fe}] = 0.4$
- iv) $[\text{Fe}/\text{H}] \leq -3.0$, $[\alpha/\text{Fe}] = 0.4$.

DSED isochrones (Dotter et al. 2008) were created for each of the chemical bins, assuming a fixed age of 12 Gyr for every bin, a mean metallicity for bins ii) and iii) and average metallicity for bins (i) and (iv) respectively. Alpha abundances were adopted for each bin as shown above. The effects of assuming a priori ages, metallicities and alpha abundances for each bin had minimal impact on the stellar parameters, as described in Section A1. The results of applying the isochrone mapping method to the entire SB02 sample are shown in Fig. 1. Thanks in part to the exquisite Gaia DR2 (Gaia Collaboration et al. 2018) data for these stars and their close proximity, it is clear from Fig. 1 that there are no dwarf-giant degenerate solutions for any of the stars. The two outlying points from the second and third bins seen in Fig. 1 have large associated uncertainties in reddening (e.g., $E(B - V) = 0.50 \pm 0.46$ from the Green et al. (2019) map).

Average differences between our redetermined stellar parameters and those from SB02 are shown in Table 1 for each bin, where this study is denoted “MV19”. The results show significant trends with metallicity in the determination of effective temperatures, where the most metal-poor bin shows the largest disagreement in temperature (and $\log g$) between the two studies.

The source of the disagreement between the two studies could be due to (1) local minima associated with the determination of the spectroscopic stellar parameters, (2) the estimated values of reddening, and/or (3) inappropriate isochrone parameters ($[\text{Fe}/\text{H}]$, age or alpha abundance). In regards to the first point, as described in Appendix A2, standard 1D LTE methods (including those used by SB02) rely on minimizing the Fe I abundance vs. excitation potential to derive the best-fit value of effective temperature. Although a unique solution is sought through the exploration of a grid of

³ <https://gea.esac.esa.int/archive/>

Table 2. Target information for our seven test case stars. Star naming scheme from the Lowell Proper Motion Survey (Giclas et al. 1971, 1978). Two separate observations of G037-037 were made and co-added for the final SNR determinations.

Star	Instrument Used	Date Observed (MJD)	R. A. (J2000)	Decl. (J2000)	<i>V</i>	<i>K</i>	Exposure (s)	S/N (6500 Å)
G184-007	HIRES	51066.371	18:24:13.099	27:17:10.896	14.42	12.33	3600	115
G189-050	HIRES	51067.459	22:56:27.490	33:53:04.200	13.94	11.74	1800	180
G158-100	HIRES	51066.538	00:33:54.600	-12:07:58.908	14.89	13.02	3600	135
G262-021	HIRES	51066.429	20:35:25.560	64:54:04.716	13.94	11.74	3600	125
G233-026	GRACES	57242.618	22:39:56.351	61:43:07.561	11.98	10.03	3600	400
G037-037	GRACES	57373.329	03:23:38.352	33:58:30.310	11.89	10.71	1800	280
...	...	57373.352	1800	...
G241-004	GRACES	57247.556	22:21:21.350	68:27:49.608	12.91	10.83	2250	20

stellar atmospheres, it is not guaranteed, due to either the grid sizing or resolution. The second and third points are discussed in Section A1; to summarize, the isochrone ages lead to the largest uncertainties in the stellar parameters, however these uncertainties are small. We suggest that the updated atomic data and modern model atmospheres have resulted in the offsets between studies, providing new and improved parameters that we adopt for the remainder of this analysis.

Finally, the effect of our new stellar parameters on metallicity shows a increase of $\Delta[\text{Fe}/\text{H}] = +0.5$ dex for stars in the lowest metallicity bin (bin 4), a $+0.2$ dex for stars in bin 3, and negligible increases for stars in bin 2. This includes NLTE effects. For the remainder of this work, we acknowledge the offsets in metallicity between our study and that of SB02 for stars in the lowest metallicity bins.

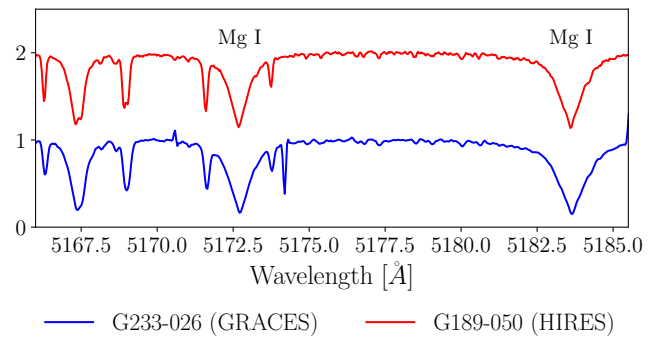
2.2 Spectral Analysis of an SB02 Subset

Significant improvements have been made in the field of stellar model atmospheres since SB02. In particular, model atmospheres now include 1D, 3D, and $\langle 3D \rangle$ radiative transfer, spherical extension, and overall improvements in our understanding of continuous and line opacities and broadening mechanisms. Additionally, significant improvements have occurred in the precision of the atomic data (energy levels, oscillator strengths, hyperfine structure components, and non-LTE line corrections). Overall, these improve the precision in the absolute abundances of elements determined from the emergent stellar spectra.

From the original SB02 sample, we selected a subset of stars for an updated detailed model atmospheres analysis, after applying additional selection criteria. The additional selection criteria were as follows:

- Orbits with $R_{\text{apo}} > 20$ kpc,
- Metallicities $[\text{Fe}/\text{H}] < -1.4$ dex, and
- Alpha-challenged with $[\alpha/\text{Fe}] < +0.2$.

The seven stars that satisfied these criteria are listed in Table 2. Four of the seven stars had existing Keck HIRES (Vogt et al. 1994) spectra in the Keck archive, to study the remaining three we obtained new observations using the Gemini Remote Access to CFHT ESPaDOnS Spectrograph (GRACES) facility (Chene et al. 2014). A summary of the observation dates, target coordinates, magnitudes (*V* from

**Figure 2.** Sample spectra near the Mg b lines is shown for G233-026 (blue) from Gemini GRACES and for G189-050 (red) from Keck HIRES.

Monet et al. (2003), K_s from Cutri et al. (2003)) and total spectral signal-to-noise ratio (SNR) for all seven stars is shown in Table 2.

2.2.1 Gemini GRACES spectroscopy

Three of the SB02 stars in our subsample were observed with the Gemini GRACES spectrograph. GRACES utilizes a 270-metre long optical fibre to combine the collecting power of the 8-metre diameter mirror of the Gemini North telescope with the exquisite spectral resolution of the Canada France Hawaii Telescope ESPaDOnS spectrograph (Manset & Donati 2003). GRACES boasts a peak transmittance of 85% at 800nm, with the ESPaDOnS resolving power ranging from $R = 40,000$ to $R = 66,000$ across its 400 to 1,000 nm wavelength range. The GRACES spectra were collected in two fibre mode to yield better sky subtraction and observed over the course of three nights between August and December of 2015. The resulting spectra displayed higher SNR at blue wavelengths (4500 Å) than expected, given the long optical fibre coupling of GRACES.

The GRACES data were reduced using the IDL reduction pipeline DRAGRACES (DR) (Chené 2017) in two fibre mode using standard calibration images. The wavelength solution was calculated within DR using the relevant ThAr arcs. The 45th order could not be recovered for all three stars, and was left as a gap in the eventual 1D continuum-normalized spectra. The final output from DR was a multi-extension fits file containing the recovered orders for both

Table 3. Stellar Parameters determined using MOOG, prior to applying non-LTE corrections, are shown in the first line for each star. Stellar parameters determined by MOOG after applying non-LTE corrections are shown in the second line (unless negligible). Gaia DR2 stellar parameters are listed in the third line as available, alongside the log g values determined using the isochrone-mapping method described in Section A1. The weighted isochrone-determined effective temperatures are given in brackets beside Gaia value. Finally, values determined by SB02 are given in the last line. Values carried forward in future analysis are in bold.

Star	Method	T_{eff} (K)	log g (cm/s^2)	M/M_{\odot}	[Fe/H]	ξ (km/s)	V_{rad} (km/s^{-1})
G037-037	LTE	6000 ± 200	3.8 ± 0.3	...	-2.35 ± 0.14	1.4 ± 0.4	-142.99 ± 0.40
	NLTE	-1.96 ± 0.19
	Gaia/DSED	5947 (6463 ± 113)	4.41 ± 0.04	0.74 ± 0.04	...	1.4 ± 0.1	-136.07 ± 3.50
	SB02	5990 ± 87	3.76 ± 0.24	...	-2.36 ± 0.06	1.54 ± 0.12	-136.3 ± 0.4
G158-100	LTE	5200 ± 200	4.6 ± 0.1	...	-2.36 ± 0.13	0.7 ± 0.5	-360.6 ± 1.1
	NLTE	-2.24 ± 0.15
	Gaia/DSED	5321 (5346 ± 57)	4.71 ± 0.01	0.60 ± 0.01	...	0.6 ± 0.1	...
	SB02	4981 ± 71	4.16 ± 0.40	...	-2.52 ± 0.08	0.50 ± 0.32	-357.9 ± 1.1
G184-007	LTE	5000 ± 200	4.5 ± 0.2	...	-1.77 ± 0.14	0 ± 0.5	-370.64 ± 0.5
	NLTE	-1.67 ± 0.14
	Gaia/DSED	5203 (5132 ± 77)	4.71 ± 0.01	0.58 ± 0.01	...	0.5 ± 0.1	...
	SB02	5147 ± 90	4.9 ± 0.5	...	-1.59 ± 0.12	0.0 ± 0.5	-371.7 ± 0.5
G189-050	LTE	5400 ± 200	4.5 ± 0.2	...	-1.43 ± 0.13	0.2 ± 0.3	-320.9 ± 0.6
	NLTE	-1.41 ± 0.15
	Gaia/DSED	5412 (5463 ± 110)	4.63 ± 0.01	0.65 ± 0.02	...	0.8 ± 0.1	-322.0 ± 1.20
	SB02	5254 ± 82	4.32 ± 0.28	...	-1.46 ± 0.06	0.3 ± 0.3	-320.7 ± 0.6
G233-026	LTE	5400 ± 300	4.5 ± 0.2	...	-1.53 ± 0.14	1.1 ± 0.3	-318.63 ± 0.64
	NLTE	-1.34 ± 0.15
	Gaia/DSED	5473 (5503 ± 62)	4.63 ± 0.01	0.64 ± 0.02	...	0.8 ± 0.1	-312.31 ± 2.04
	SB02	5303 ± 59	4.39 ± 0.26	...	-1.45 ± 0.06	0.64 ± 0.18	-313.6 ± 0.6
G262-021	LTE	5100 ± 300	4.3 ± 0.2	...	-1.37 ± 0.13	0.4 ± 0.4	-214.0 ± 0.5
	NLTE	-1.37 ± 0.16
	Gaia/DSED	5096 (5140 ± 81)	4.67 ± 0.01	0.60 ± 0.01	...	0.6 ± 0.1	...
	SB02	4985 ± 56	4.26 ± 0.38	...	-1.45 ± 0.09	0.00 ± 0.50	-214.5 ± 0.5

the science and sky fibres. As a final step in the reduction, the sky was subtracted and continuum normalized using a k-sigma clipping routine. In the case G037-037, two independent spectra were stacked and re-normalized. Heliocentric corrections were applied following reduction using the IRAF `rvcorrect` task. Radial velocity corrections were performed using the IRAF `fxcor` routine from lines in the proximity of the $H\alpha$ and the Mg b lines (near 518 nm); results are shown and compared with SB02's radial velocities in Table 3.

Unfortunately, the SNR of the sky-subtracted spectrum for the star G241-004 was too low for further analysis.

2.2.2 Keck HIRES (archival) spectroscopy

Spectra for the remaining four stars in our subsample were retrieved from the Keck Observatory Archive⁴. The spectra were taken with HIRES (Vogt et al. 1994) during the SB02 observing campaign, which ran from July 1995 to September 1998. SB02 noted that the spectrometer set up did not change appreciably from run to run; they selected the C1 decker to define the slit dimensions as $0.861''$ wide by $7.0''$ long and used a KV408 order blocking filter to eliminate contamination from neighboring diffraction orders. The HIRES red collimator/camera and the Tek 2048 CCD were used to

gather spectra from 450 to 680 nm, with small inter-order gaps redward of 500 nm.

Similar to SB02, we used standard IRAF reduction methods as in `noao.imred.echelle`. Science images were de-biased, flattened and trimmed to account for the overscan regions. Sky subtraction was performed during the 1D extraction and bad pixels were identified and removed. Wavelength solutions were created using the corresponding ThAr spectra and used to calibrate the final 1D spectra. Radial velocity corrections were applied using the IRAF `dopcorr` task and heliocentric corrections using the same method as the GRACES data. The 1D spectra were continuum normalized using k-sigma clipping.

3 STELLAR ABUNDANCES

Stellar parameters for our subset were determined from two methods: (1) spectroscopic parameters using classical methods involving the Fe I and Fe II spectral lines, and (2) the Gaia DR2 parallaxes, colour temperatures, and DSED isochrones using the same technique as in Section 2.1 and described in Section A1. We adopt the latter technique for our final parameters but discuss both, including error analysis, in Appendix A. The results of both studies are given in Table 3 with the final stellar parameters shown in bold.

Following the stellar parameter determinations, model

⁴ <http://nexsci.caltech.edu/archives/koa/>

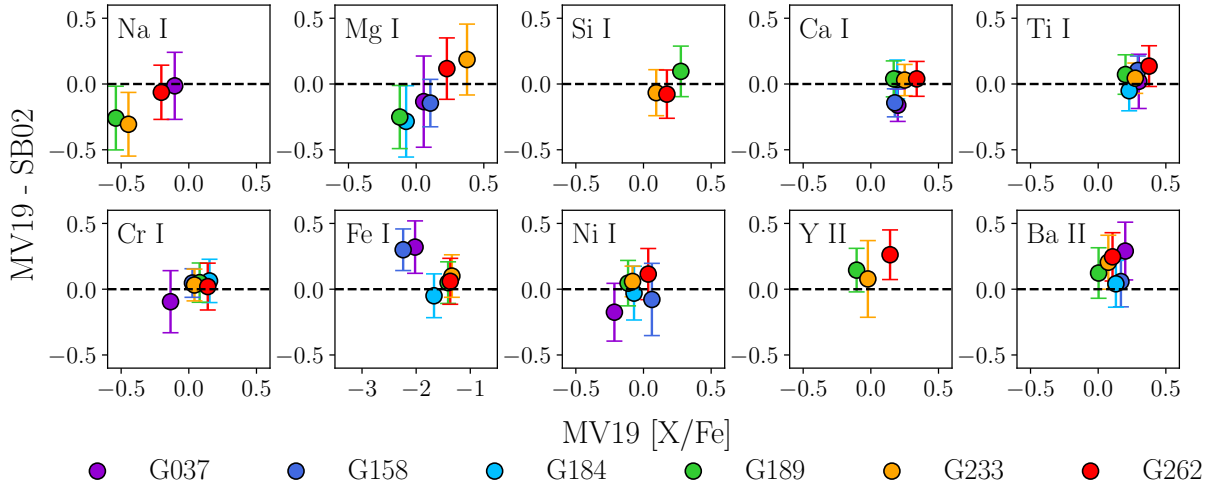


Figure 3. A comparison of the element abundances $[X/Fe]$ between our analysis “MV19” and SB02 for six stars. The x-axis is $[X/Fe]$, except for Fe I where $[Fe I/H]$ is used. Abundances are listed in Table C1.

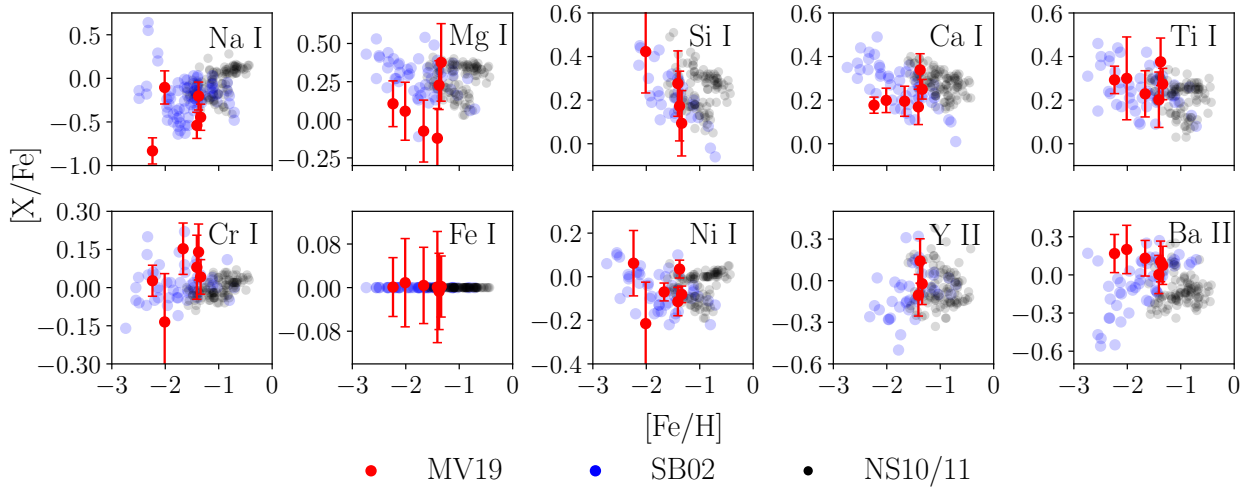


Figure 4. Comparison of the abundances from SB02 (blue), NS10/11 (black), and our analysis of the six stars in our subset (“MV19”, red) for 10 elements in common.

atmospheres were generated using the MARCS (Gustafsson et al. 2003, 2008, further expanded by B. Plez) and ATLAS models (Kurucz 2005). Spectral lines and atomic data were gathered from SB02, Norris et al. (2017), and Battaglia et al. (2017) after limiting the range of exploration to the overlapping wavelength regimes of the HIRES and GRACES data ($\sim 4200 - 6700 \text{ \AA}$). Atomic data were updated when appropriate by comparing to the *linemake*⁵ atomic and molecular line database. Equivalent width (EW) measurements and abundance determinations were automated using DAOSpec (Stetson & Pancino 2008) and the 1D, LTE stellar analysis

code MOOG (Snedden 1973). For further details regarding the EW analysis please see Section A2.1.

Relative abundances were calculated for each star using the Asplund et al. (2009) solar data as a comparison and are listed Table C1. Abundance errors were calculated from the dispersion in the EW determinations (σ_{EW}) and the uncertainty in abundances found from varying each of the stellar parameters; effective temperature $T_{eff} \pm 100K$ (σ_{Teff}), gravity $\log g \pm 0.3 \text{ dex}$ (σ_{logg}), metallicity $[Fe/H] \pm 0.5 \text{ dex}$ ($\sigma_{[Fe/H]}$) and microturbulence $\chi \pm 0.2 \text{ km/s}$ (σ_{χ}). Each stellar parameter uncertainty was then scaled by the uncertainty in the isochrone mapped stellar parameters assuming a linear relationship before being added in quadrature to generate a conservative estimate of the effect of stellar parameter uncertainties $\sigma_{SP, TOT} = \sqrt{\sigma_{Teff}^2 + \sigma_{logg}^2 + \sigma_{[Fe/H]}^2 + \sigma_{\chi}^2}$. The final uncertainty in $[Fe/H]$ was determined by adding the solar Fe I uncertainty to the absolute Fe I abundance in quadrature ($\sigma_{Fe I}$). Overall, the final uncertainties (σ_{EW} , $\sigma_{SP, TOT}$,

⁵ *linemake* contains laboratory atomic data (transition probabilities, hyperfine and isotopic substructures) published by the Wisconsin Atomic Physics and the Old Dominion Molecular Physics groups. These lists and accompanying line list assembly software have been developed by C. Sneden and are curated by V. Placco at <https://github.com/vmplacco/linemake>.

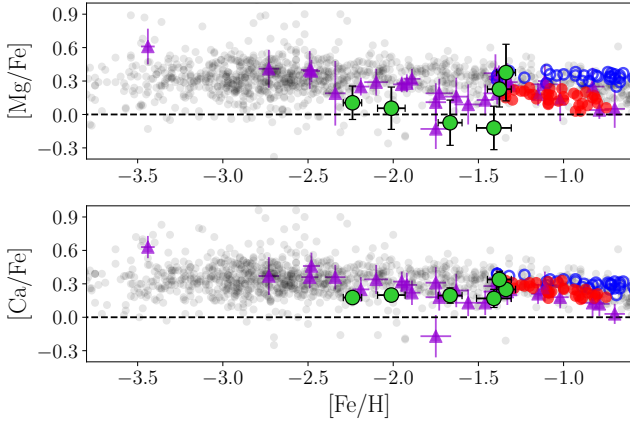


Figure 5. Alpha abundances for our re-analysed SB02 stars (green), the entire SB02 sample (purple triangles), low alpha (red) and high alpha (blue) stars from NS10/11 (Nissen & Schuster 2010, 2011), and halo stars (grey; Yong et al. 2013, Berg et al. 2016, Venn et al. 2004).

$\sigma_{\text{Fe I}}$) are added in quadrature, assuming each uncertainty is independent.

3.1 Comparing with SB02

As we have not reanalysed the entire SB02 sample, we now investigate the validity of assuming the original SB02 abundances for the remaining 49 stars. The abundance determinations for stars in common between the two studies, ours (“MV19”) and SB02 are compared after removing differences in the adopted solar abundances. This is done by determining the offset between the solar data used in SB02 (Grevesse & Anders 1989) and our adopted solar abundances from Asplund et al. (2009). Offsets were applied to all elements in common with the largest offset applied to the Grevesse & Anders (1989) value of Na I (+0.09 dex). The normalised comparisons are presented in Fig.3, where the difference in measured abundances are plotted as a function of our “MV19” measurements. Note that not all six stars appear in each elemental subplot, this is due to missing abundance measurements for that star in one or both of the studies.

In general, there is 1σ agreement between the two studies for all six stars in common across all the elements. Exceptions to this are the abundances Na I, Mg I, Fe I, and Y II for select stars. Regarding the Fe I disagreement, the most metal poor stars (G037-037, G158-100) show the biggest disagreement in Fe I. This is expected due to larger disagreements in $\log g$ (~ 0.6) and temperature (~ 400 K, see Section 2.1). We cannot explain the Y II disagreement seen in G262-021 as it is not attributed to differences in atomic lines or atomic data. The remaining abundance disagreements for the four stars in our sample with low Mg as well as the one Na-poor star are discussed in the subsequent section.

3.2 Comparing with NS10/11

To examine the abundance disagreements in Na I and Mg I further, we compare abundances with the high-velocity, intermediate metallicity ($[\text{Fe}/\text{H}] > -1.6$) stars examined by

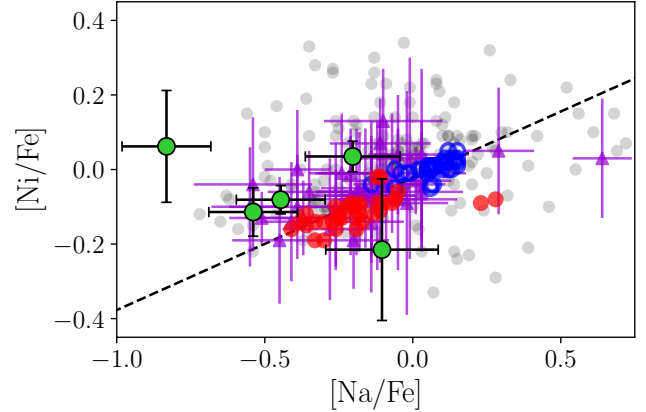


Figure 6. Na-Ni correlation found by NS10/11 for the three studies, using the same labels as in Fig. 5. We note that the three points from this paper (green) that are closest to the Ni-Na line are also Mg-poor stars.

Nissen & Schuster (2010, 2011). In Fig.4, effects due to difference in the solar abundances are taken into account, however we could not shift the NS10/11 data due to their differential abundance methodology. We note that in Fig. 4, no systematic offsets are seen between the three studies. As discussed in the previous section, the four stars in our sample with low Mg stand out, as well as the one Na-poor star. Otherwise, our results overlap with both the NS10/11 sample near $[\text{Fe}/\text{H}] = -1.5$ and the entire SB02 sample to within 1σ . Otherwise, our results overlap with both the NS10/11 sample near $[\text{Fe}/\text{H}] = -1.5$ and the entire SB02 sample to within 1σ .

As a reminder, alpha-challenged stars were favoured by the additional selection criterion when choosing our six stars (see Section 2.1), therefore we expect these stars are truly low in $[\text{Mg}/\text{Fe}]$. In addition, SB02 did not measure a $[\text{Na}/\text{Fe}]$ abundance for G158-100 as they chose to reject lines with an equivalent width (EW) $> \sim 85\text{\AA}$ around 5650\AA . The measured Na I line for G158-100 occurs at $\sim 5895\text{\AA}$ and is within our accepted EW range ($< 150\text{\AA}$, see Section A2), thus we identify this star as truly Na-poor.

Alpha abundances ($[\text{Mg}/\text{Fe}]$ and $[\text{Ca}/\text{Fe}]$) are examined in more detail relative to the NS10/11 sample in Fig. 5. NS10/11 found two distinctly different groups of stars based on a differential abundance analysis and detailed kinematics: stars with high alpha abundances show halo kinematics (blue), and alpha-poor stars have high or retrograde velocity orbits (red). Not only are the majority of our six stars and the rest of the SB02 sample more metal-poor than NS10/11, but our Mg-poor stars do not fit with either of the NS10/11 groups. If the low-alpha stars in the NS10/11 sample have been accreted from a dwarf galaxy, our four Mg-poor stars from the SB02 sample are from a different accretion event (or events). Finally, we note that even with our conservative estimates of the abundance uncertainties, our measurements are more accurate than those of the original SB02 study - highlighting the importance of updating the atomic data and stellar atmospheres.

NS10/11 also found that the $[\text{Ni}/\text{Fe}]$ and $[\text{Na}/\text{Fe}]$ abundances were correlated but offset between their two groups;

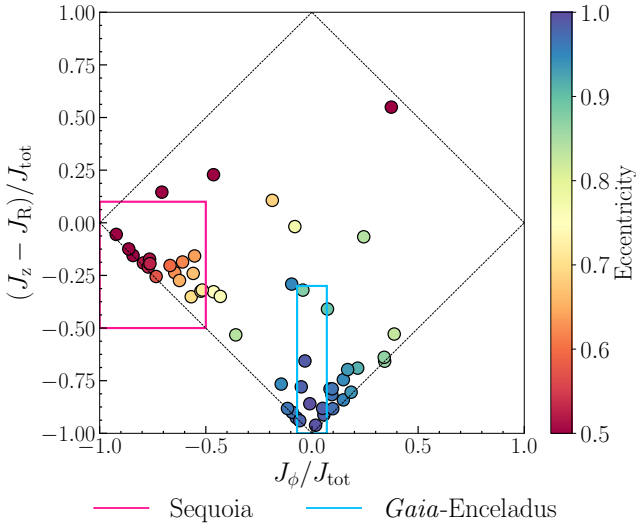


Figure 7. Action map of the entire SB02 sample. The horizontal axis shows the J_ϕ action, and the vertical axis shows the difference between the vertical and radial action, with both axes normalized by the total action. The approximate locations of the *Gaia*-Enceladus (blue box) and *Gaia*-Sequoia (pink box) events are identified as determined by (Myeong et al. 2019).

see Fig. 6. The Ni and Na abundances in the SB02 sample are in agreement with the NS10/11 sample, and we note that three stars with low Mg abundances are also aligned with this correlation (neglecting the two outliers from our sub-sample). In fact, our three Mg-poor stars appear to be better agreement with the low-alpha (accreted) stars in the NS10/11 sample, i.e., lower [Na/Fe]. The offset above the line towards higher [Ni/Fe] (or equivalently lower [Na/Fe]) appears to be a systematic error, possibly related to updates in the atomic data.

4 STELLAR DYNAMICS

It has been demonstrated recently that the best way to identify stars belonging to discrete merger events such as *Gaia*-Enceladus or *Gaia*-Sequoia, is by using their characteristic dynamical properties, namely the orbital actions, which retain the signature of the event over long time periods (Myeong et al. 2018a,b, 2019). Here we calculate dynamical properties of the SB02 sample in order to investigate potential associations with ancient merger events. Parallaxes, proper motions, and the respective errors on these quantities were obtained from the Gaia DR2 archive, and are shown in Appendix B.

To determine the dynamical properties, we adopt the potential of McMillan (2017), the characteristics of which are described in Tables 1 and 4 of that work. Celestial coordinates are transformed to galactocentric coordinates assuming the following: the location of the galactic center is (RA = 17:45:37.224 h:m:s, Dec = -28:56:10.23 degrees) (Reid & Brunthaler 2004); The Sun is 20.8 pc above the galactic plane (Bennett & Bovy 2019) and the solar peculiar velocity is $(U, V, W) = (11.1, 12.24, 7.25)$ km/s (Schönrich et al. 2010). The distance to the solar circle, and the circular velocity at

that radius are 8.121 kpc (Gravity Collaboration et al. 2018) and 229 km/s (Eilers et al. 2019) respectively, which are both quite similar to the intrinsic values of the McMillan (2017) potential. Note that we use a left handed coordinate system such that, from the position of The Sun, galactocentric X, Y, and Z are positive towards galactic anti-center, the direction of galactic rotation, and the galactic north pole respectively. Orbital integrations were performed using a 4-D symplectic integrator implemented in GALPY, a galactic dynamics Python package (Bovy 2015). All orbits were integrated for a total of 10 Gyr (± 5 Gyr) with select orbits shown in Appendix B.

4.1 *Gaia*-Enceladus and *Gaia*-Sequoia

The actions J_ϕ , J_r and J_z of the SB02 sample were calculated using an implementation of the Stäckel fudge method in GALPY (Binney 2012; Mackereth & Bovy 2018). Fig. 7 shows our sample in action space, where the horizontal axis shows the ϕ action (equivalent to L_z) and the vertical axis shows the difference between the vertical and radial actions. Both axes are normalized by the absolute sum of the actions: J_{tot} . We label the *Gaia*-Enceladus and *Gaia*-Sequoia accretion events following Myeong et al. (2019). While it broadly appears that our sample is dominated by stars populating these two regions, the selection criteria that define our sample undoubtedly plays a role in sculpting the appearance of the distribution. Each star in Fig. 7 is coloured by its eccentricity, and in general we see that stars in the *Gaia*-Enceladus selection box have $e > 0.9$ and those in the *Gaia*-Sequoia selection box have $e \sim 0.5 - 0.6$, which is as expected.

The Gaia data for the SB02 sample was filtered to remove stars with $BP - RP > 2$ and $phot_bp_rp_excess > 1.4$ in Fig. 7. Stars with large $astrometric_chi2_al$ values, indicating a poor astrometric solutions, were also removed. These cuts follow from Arenou et al. (2018), who recommend astrometric solutions with large $astrometric_chi2_al$ values be avoided, while values of $phot_bp_rp_excess_factor$ should be around one for normal stars. Interestingly, the star that displays the most circular orbit (shown as the star closest to the top vertex), G025-024, has normal astrometric parameters, suggesting that is in-fact unique dynamically from the remaining stars in the sample.

In our subset of six SB02 stars, G262-021 and G233-026 are classified as belonging to the *Gaia*-Enceladus accretion event, while G158-100 and G184-007 are identified as belonging to the *Gaia*-Sequoia event. For the remaining stars in the SB02 sample, we only identify stars found entirely within the action-space bounds as possible members of each accretion event. In total 9 SB02 stars are classified as *Gaia*-Enceladus stars, and 17 are classified as *Gaia*-Sequoia stars.

4.2 Chemodynamics of the SB02 sample

The distribution of the SB02 sample is shown on the Toomre diagram and in angular momentum vs. energy space (L_z vs. E) in Fig. 8. Values of L_z and E shown are normalized by the solar values from the McMillan (2017) potential ($L_{z\odot} = 2014.2$ kpc km/s and $E_\odot = -1.54 \times 10^5$ km²/s²). In the Toomre diagram, it is clear that the majority of the SB02 sample

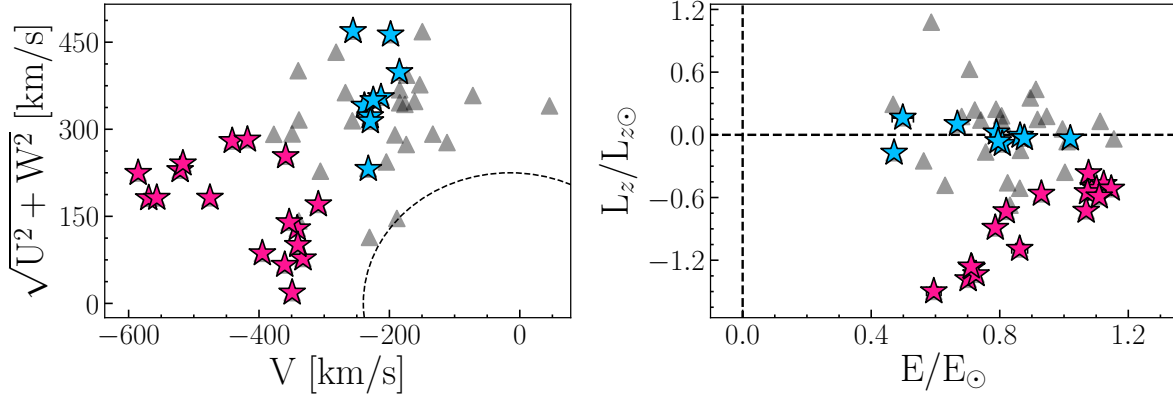


Figure 8. Toomre diagram (*left*) showing stars in the SB02 sample. Those associated with the *Gaia*-Enceladus merger (sky blue stars), the *Gaia*-Sequoia event (pink stars), or simple outer halo stars (grey) are identified. Angular momentum and energy (*right*) are scaled by the (McMillan 2017) potential solar values ($L_{z\odot} = 2014.2$ kpc km/s and $E_{\odot} = -1.54 \times 10^5$ km²/s²). The dashed line represents stars with thin disk dynamics ($V_{\text{circ}} = 229$ km s⁻¹).

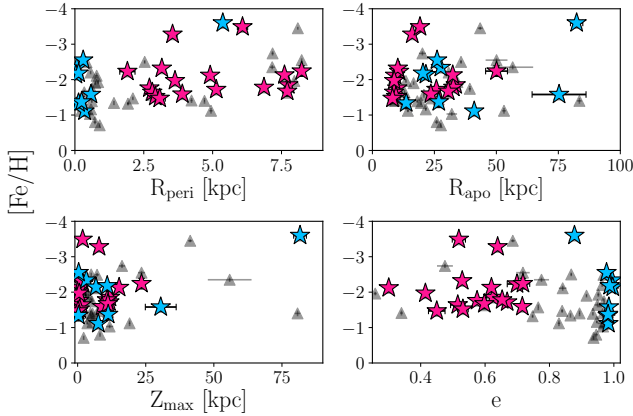


Figure 9. Metallicity distribution as a function of various orbital parameters derived in Section 4. Data is presented using the convention of Fig. 8.

are high halo stars or highly retrograde orbits, confirming the initial kinematic cuts made by SB02. A clear separation between the *Gaia*-Enceladus and *Gaia*-Sequoia stars is also seen, as is expected given their unique dynamical signatures. In L_z vs E space the *Gaia*-Sequoia stars are more distinct with highly retrograde orbits, while *Gaia*-Enceladus stars straddle the line of zero angular momentum, which reflects the radially biased orbits of its constituent stars. While we employ a different potential than Helmi et al. (2018), the broad trends which describe the kinematics of these merger events remain.

The distribution of metallicity is examined as a function of several orbital parameters in Fig. 9, including pericentric radius (R_{peri}), apocentric radius (R_{apo}), maximum height from the disk (Z_{max}) and eccentricity (e). While both events show unique dynamic signatures, no obvious chemodynamic trends are found. For example, if the outer parts of the accreted systems were stripped first, then the location of associated member stars within the MW potential could probe the existence of an original metallicity gradient in the progenitor. Either these systems were small enough that no

metallicity gradient existed, or this sample is too small to test this hypothesis.

4.2.1 Chemical signatures of accretion: locating the $[\alpha/\text{Fe}]$ knee

One of the classic indicators of the star formation history in a dwarf galaxy is the metallicity of the $[\alpha/\text{Fe}]$ knee, i.e., where $[\alpha/\text{Fe}]$ begins to decrease as a function of increasing metallicity (Tolstoy et al. 2009; Venn et al. 2004). The knee is usually attributed to the onset of Type Ia supernovae, diluting the alpha abundances produced from earlier core collapse supernovae, although it may also be related to variations in the local IMF (Tinsley 1979; Matteucci & Brocato 1990; Matteucci 2003; Tolstoy et al. 2003; McWilliam et al. 2013; Fernández-Alvar et al. 2018). A slower star formation efficiency, or effectively truncated upper IMF moves the knee to lower metallicities in dwarf galaxies. Assuming that a large fraction of the SB02 stars (4/6 in our subsample and 26/54 in the entire re-analyzed sample) may be associated with one or more proposed merger events, then we examine the $[\text{Mg}/\text{Fe}]$ and $[\text{Ca}/\text{Fe}]$ ratios vs $[\text{Fe}/\text{H}]$ in Fig. 10.

For the stars we associate with *Gaia*-Enceladus, a $[\alpha/\text{Fe}]$ knee appears in both Mg and Ca at lower metallicities than the Galactic comparison stars, near $[\text{Fe}/\text{H}] \sim -1.6$; see Fig. 10. This value is in good agreement with the NS10/11 low-alpha stars, $[\text{Fe}/\text{H}] \leq -1.5$, but slightly lower than the location identified by Myeong et al. (2019) near $[\text{Fe}/\text{H}] = -1.3$ using SDSS APOGEE data and Matsuno et al. (2019) using the SAGA database ($[\text{Fe}/\text{H}] \sim -2$). For the stars that we have associated with *Gaia*-Sequoia, a $[\alpha/\text{Fe}]$ knee is much less distinct since nearly all of the associated stars have low $[\alpha/\text{Fe}]$ abundances. We determine a knee near $[\text{Fe}/\text{H}] \sim -2$, but with high uncertainty. This value is in fair agreement with Myeong et al. (2019) at $[\text{Fe}/\text{H}] \sim -1.6$ and Matsuno et al. (2019) near $[\text{Fe}/\text{H}] \sim -2.5$.

Data from the Sculptor dwarf galaxy (considered a “textbook dwarf spheroidal galaxy”, Hill et al. 2019) is compared with the SB02 and NS10/11 data in Fig. 11. The $[\alpha/\text{Fe}]$ knee in the Sculptor data is near $[\text{Fe}/\text{H}] \sim -1.8$, between our identifications for *Gaia*-Enceladus and *Gaia*-

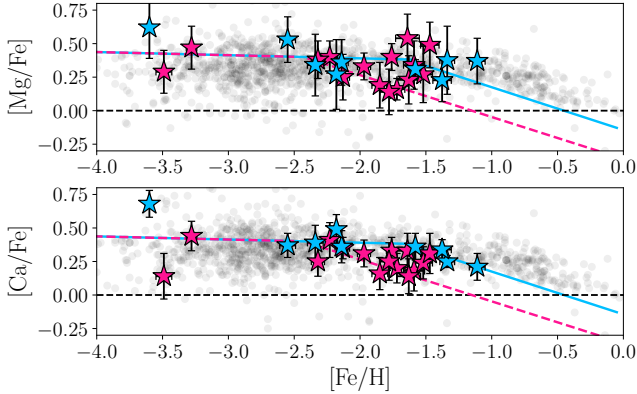


Figure 10. Alpha abundances for stars classified as part of the proposed *Gaia*-Enceladus accretion event (sky blue stars) and *Gaia*-Sequoia accretion event (pink stars). The location of the alpha knee in both the *Gaia*-Enceladus stars and the *Gaia*-Sequoia stars is plotted as the decreasing trends around $[\text{Fe}/\text{H}] \sim -1.6$ (sky blue line) and $[\text{Fe}/\text{H}] \sim -2$ (pink dashed line) respectively. Halo stars from the literature are also included as black circles (Yong et al. 2013; Berg et al. 2016; Venn et al. 2004).

Sequoia. Drawing tentative conclusions from Figs. 10 and 11, the *Gaia*-Enceladus and *Gaia*-Sequoia stars do appear to occupy unique chemo-dynamical spaces, also indicating different star formation histories that are similar to those of other dwarf galaxies.

4.2.2 Chemical signatures of accretion: Ni-Na correlation

Another space in which to probe possible chemical accretion signatures is the Ni-Na space, discussed in Section 3.2. As seen in Fig. 6, the majority of the SB02 stars follow the same Ni-Na trend as the NS10/11 low-alpha stars. When splitting the stars into potential *Gaia*-Enceladus and *Gaia*-Sequoia associated stars, no obvious differences were seen between the two subsets. Both subsets have outliers from the trend seen in Fig. 6, such as Na-rich stars (also reported by NS10/11). The comparisons of the Na-Ni abundances for the *Gaia*-Enceladus and *Gaia*-Sequoia associated stars is inconclusive. When Sculptor data is also examined, most stars do not fall on the Na-Ni trend, but those abundances also have significantly larger errors, i.e., fainter objects than in our analysis or NS10/11.

4.3 Other interesting stars

In this section, we discuss other interesting stars that are not kinematically associated with the *Gaia*-Enceladus or *Gaia*-Sequoia events.

4.3.1 The chemically peculiar star G251-024

This star is BD +80°245, previously discovered and analysed by Fulbright (2002) and Ivans et al. (2003). Both groups found low α and Ba abundances, which we confirm in this study ($[\text{Mg}/\text{Fe}] = -0.11 \pm 0.18$, $[\text{Ca}/\text{Fe}] = -0.19 \pm 0.19$, $[\text{Ti}/\text{Fe}] = -0.27 \pm 0.11$, and $[\text{Ba}/\text{Fe}] = -1.37 \pm 0.18$). Ivans et al. (2003) also found it is low in the r-process element

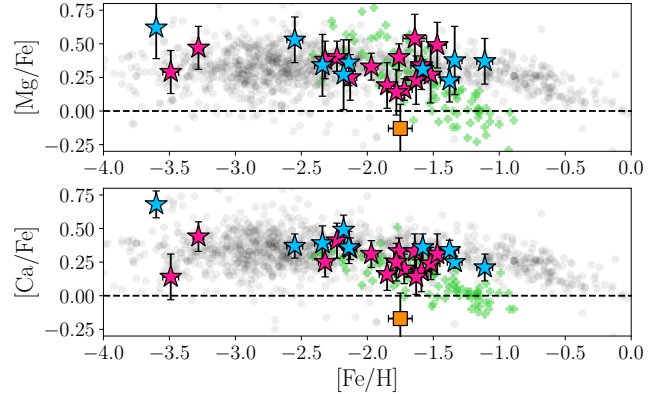


Figure 11. Same as Fig. 10 with the addition of the Sculptor data (Hill et al. 2019) and the chemically peculiar star G251-024.

$[\text{Eu}/\text{Fe}] = -0.64 \pm 0.18$, and several others. We highlight this star in Fig. 10 as an orange square, to show how distinct its chemistry is from the main sample and all other chemo-dynamical groups. This star was compared to the chemically unique star Car-612 found by Venn et al. (2012) in the Carina dwarf galaxy. It was proposed then that these stars are unusual due to enhancements in the iron-group elements, e.g., possibly forming in a pocket of SN Ia products that dilutes $[\text{X}/\text{Fe}]$ abundances locally. This was further explored for a larger number of stars in Carina by Norris et al. (2017), and implies inhomogeneous mixing of the interstellar medium at early times in low mass dwarf galaxies.

Unfortunately this star has the worst astrometry in the entire SB02 sample. The Gaia parameters, `astrometric_chi2_al` and `phot_bp_rp_excess_factor` have values of ~ 2311 and ~ 1.49 respectively, inhibiting further chemo-dynamic analysis.

4.3.2 Li in G037-037

G037-037 is the only star in our sub-sample hot enough (6000 K) to have preserved its initial Li abundance, protected from destruction by convection (see Spite & Spite (1982b) and references within). Spectrum synthesis of the Li I 6707 Å line (including hyperfine structure components and NLTE corrections) results in $A(\text{Li}) = 2.16 \pm 0.10$ dex. The Spite Plateau (Spite & Spite 1982a,b) is identified by Meléndez & Ramírez (2004) near $A(\text{Li}) = 2.37$ dex, however in the metallicity range ($[\text{Fe}/\text{H}] \sim -2.5$) of turn-off stars ($\log g \geq 3.7$) like G037-037, the Lithium Plateau is identified by Aguado et al. (2019, and references therein) at $A(\text{Li}) = 2.2$ dex, in good agreement with our result. Aguado et al. (2019) suggest that such uniformity in the metal-poor stars as a result of depletion from a higher initial Li abundance seems unlikely, possibly pointing to new physics.

4.3.3 The Mg-poor stars: G184-100 & G189-050

In Fig. 5, two of the stars that we reanalysed have lower $[\text{Mg}/\text{Fe}] \sim -0.1$ than in SB02, yet their $[\text{Ca}/\text{Fe}] \sim +0.2$. The α -elements form through hydrostatic H- and He-core burning stages, though some Ca can also form later during SN Ia

events. Because of these different nucleosynthetic sites, the $[\text{Mg}/\text{Ca}]$ ratio need not scale together at all metallicities. Rarely do stars have sub-solar $[\text{Mg}/\text{Fe}]$, however such stars have been found in some dwarf galaxies, e.g., the Carina and Sextans dwarf galaxies (Norris et al. 2017; Jablonka et al. 2015; Venn et al. 2012), the Tri II ultra faint dwarf galaxy (Venn et al. 2017), as well as the unusual star cluster NGC 2419 (Cohen & Kirby 2012). In NGC 2419, the low Mg abundances is (anti-)correlated with other elements (K and Sc). Combining this result with its unusual retrograde orbit, Cohen & Kirby (2012) suggested that NGS 2419 is not a globular cluster, but rather the core of an accreted dwarf galaxy. Our spectra do not extend to the $\text{K I } 7699 \text{ \AA}$ line, and we do not find offsets in our Sc II abundances when compared to Galactic halo stars with similar metallicities, however one of these two stars, G184-100, is dynamically associated with *Gaia*-Sequoia.

4.3.4 G122-051: A metal weak thick disk star?

G122-051, a member of the original SB02 sample, is a prograde star in a highly elliptical, planar orbit ($Z_{\text{max}} < 0.17 \text{ kpc}$, $R_{\text{apo}} = 19.6 \text{ kpc}$, and $e = 0.87$). Using the solar values stated in Section 4, we find that the azimuthal velocity of G122-051 is $+108 \text{ km s}^{-1}$. Comparing this azimuthal velocity with that of the three proposed MW components; halo, thick and thin disks and considering its chemistry, $[\text{Fe}/\text{H}] = -1.34 \pm 0.06$ and $[\alpha/\text{Fe}] = 0.26 \pm 0.05$, then G122-051 is not clearly an outer halo star. A better description is that it is a member of the proposed *metal weak thick disc* (MWTD) (Chiba & Beers 2000; Beers et al. 2002), where the mean MWTD azimuthal velocity in Carollo et al. (2010) is $V_{\phi} = 100 - 150 \text{ km s}^{-1}$ and mean metallicity $[\text{Fe}/\text{H}] \sim -1.3$.

Similarly, the MWTD parameters from Kordopatis et al. (2013) again associate this star most closely with the MWTD ($V_{\phi} = 123 \pm 16 \text{ km s}^{-1}$ and $[\text{Fe}/\text{H}] \sim -1.6$). Alternatively, using the convention of Hayes et al. (2018) this star is classified a high Mg star, $[\text{Mg}/\text{Fe}] \sim +0.3 \text{ dex}$, where its motion also agrees with the high Mg population ($V_{\text{phi}} \sim 120 - 150 \text{ km s}^{-1}$). Although, Hayes et al. (2018) do not claim that their high-Mg population is related to the MWTD, they do suggest that they could be related.

The existence of a MWTD as a separate chemodynamic component of the MW thick disc is still the subject of debate. In some studies, a separate metal weak component of the thick disc is needed to fit the observed rotational properties of low-metallicity stars like G122-051 near the plane (Carollo et al. 2010; Kordopatis et al. 2013). Other studies reject the idea of discrete thick and thin discs entirely (Bovy et al. 2012), claiming that the MW has only one disk which can be explained well with a singular mass distribution varying as a function of scale height. When treated as a discrete component of the MW disk, the MWTD is generally suggested to have formed in-situ, with contributions from mergers dynamically heating the precursor MWTD to the scale height seen today (Hayes et al. 2018; Haywood et al. 2018; Di Matteo et al. 2018).

In their chemodynamic study of MW halo stars, Di Matteo et al. (2018), found that only about 25% of stars in the metallicity range $-1.5 \leq [\text{Fe}/\text{H}] \leq -1.0$ and Mg-abundance range $0.25 \leq [\text{Mg}/\text{Fe}] \leq 0.35$ are accreted stars - suggesting G122-051 perhaps formed in-situ. However, they also

note the appearance of a peak in the number of stars found near $V_{\phi} \sim 100 \text{ km s}^{-1}$ (translated to our coordinate system) in the aforementioned metallicity and Mg-abundance range. They suggest this concentration of stars, which again includes G122-051, could either be accreted in an event that results in a variety of deposited orbits, or denote the separation between the MWTD and the remainder of the thick disk.

5 CONCLUSIONS

We have re-examined the Stephens & Boesgaard (2002) data set of “outer halo stars” on energetic or highly retrograde orbits, using *Gaia* DR2 astrometry and high resolution Keck HIRES and Gemini GRACES spectra. Stellar parameters and abundances have been updated for six stars in the sample, using new model atmospheres and updated atomic data from which we confirm the low metallicities of these objects.

When combined with *Gaia* DR2 data, we find that nine stars in the SB02 sample are dynamically coincident with the *Gaia*-Enceledas satellite merger, including one very low metallicity star (G238-030) ($[\text{Fe}/\text{H}] \sim -3.6$). We also find 17 stars that are dynamically coincident with the *Gaia*-Sequoia accretion event, including one very metal-poor star near $[\text{Fe}/\text{H}] = -3.5$. Both metal-poor stars have low masses and isochrone ages older than 10 Gyr. A knee in $[\alpha/\text{Fe}]$ is found in the *Gaia*-Enceladus stars, near $[\text{Fe}/\text{H}] \sim -1.6$, however it is less clear in the *Gaia*-Sequoia sample, potentially occurring around $[\text{Fe}/\text{H}] \sim -2$. These are consistent with other analyses of the $[\alpha/\text{Fe}]$ knees in these systems based on SDSS APOGEE data. If the metal-poor stars in these samples are true members of the *Gaia*-Enceledas and *Gaia*-Sequoia remnants, they present opportunities to probe the low metallicity tail and early star formation history of these systems.

Additionally, we find several individual stars with interesting chemodynamical properties. These include two $[\text{Mg}/\text{Fe}]$ challenged stars, one of which is dynamically associated with the *Gaia*-Sequoia accretion event, and one star with $A(\text{Li}) = 2.2$ which is similar to other metal-poor, turn-off stars that define a Lithium Plateau (below the Spite Plateau). We also find one star that could be part of a metal weak thick disk in the MW.

The dynamical picture of the MW is continuously evolving thanks to the spectacular data from *Gaia*, while a chemodynamic picture of the MW is just emerging. This chemodynamic picture is set to become more clear in the upcoming era of spectroscopic surveys (SDSS-V, WEAVE, and 4MOST). Undoubtedly, the combination of detailed chemical abundances and orbital dynamics will provide the best view of the formation and accretion history of our Galaxy.

ACKNOWLEDGEMENTS

Thanks to Ken Freeman, John Norris, Rosemary Wyse, Mike Irwin, Luca Casagrande, Anke Arentsen, André-Nicolas Chené, Aaron Dotter and Jo Bovy for their invaluable advice, suggestions, isochrones and comments throughout the process. Thanks especially to Mike Irwin for the initial suggestion to examine the full dynamics of the sample - without this addition the paper would not be what

it is. S Monty acknowledges the support provided for a portion of this research by the Natural Sciences and Engineering Research Council of Canada (NSERC) Undergraduate Student Research Awards (USRA). The authors wish to recognize and acknowledge the very significant cultural role and reverence that the summit of Maunakea has always had within the indigenous Hawaiian community. We are most fortunate to have the opportunity to conduct observations from this mountain. This research made use of Astropy, <http://www.astropy.org> a community-developed core Python package for Astronomy (The Astropy Collaboration et al. 2018) and SciPy (Jones et al. 01). This work is based on observations obtained at the Gemini Observatory, which is operated by the Association of Universities for Research in Astronomy, Inc., under a cooperative agreement with the NSF on behalf of the Gemini partnership: the National Science Foundation (United States), National Research Council (Canada), CONICYT (Chile), Ministerio de Ciencia, Tecnología e Innovación Productiva (Argentina), Ministério da Ciência, Tecnologia e Inovação (Brazil), and Korea Astronomy and Space Science Institute (Republic of Korea). This research has made use of the NASA/ IPAC Infrared Science Archive, which is operated by the Jet Propulsion Laboratory, California Institute of Technology, under contract with the National Aeronautics and Space Administration. This research has made use of the Keck Observatory Archive (KOA), which is operated by the W. M. Keck Observatory and the NASA Exoplanet Science Institute (NExSci), under contract with the National Aeronautics and Space Administration.

REFERENCES

- Aguado D. S., González Hernández J. I., Allende Prieto C., Rebolo R., 2019, *ApJ*, **874**, L21
- Ahn C. P., et al., 2014, *ApJS*, **211**, 17
- Andrae R., et al., 2018, *A&A*, **616**, A8
- Arenou F., et al., 2018, *A&A*, **616**, A17
- Asplund M., Grevesse N., Sauval A. J., Scott P., 2009, *ARA&A*, **47**, 481
- Bahcall J. N., Soneira R. M., Schmidt M., 1983, *ApJ*, **265**, 730
- Bailer-Jones C. A. L., Rybizki J., Foesneau M., Mantelet G., Andrae R., 2018, *AJ*, **156**, 58
- Battaglia G., North P., Jablonka P., Shetrone M., Minniti D., Díaz M., Starkenburg E., Savoy M., 2017, *A&A*, **608**, A145
- Beers T. C., Drilling J. S., Rossi S., Chiba M., Rhee J., Fuhrmeister B., Norris J. E., von Hippel T., 2002, *AJ*, **124**, 931
- Belokurov V., Deason A. J., Koposov S. E., Catelan M., Erkal D., Drake A. J., Evans N. W., 2018a, *MNRAS*, **477**, 1472
- Belokurov V., Erkal D., Evans N. W., Koposov S. E., Deason A. J., 2018b, *MNRAS*, **478**, 611
- Bennett M., Bovy J., 2019, *MNRAS*, **482**, 1417
- Berg T. A. M., Ellison S. L., Prochaska J. X., Venn K. A., Dessauges-Zavadsky M., 2016, VizieR Online Data Catalog, *p. J/MNRAS/452/4326*
- Bergemann M., Lind K., Collet R., Magic Z., Asplund M., 2012, *MNRAS*, **427**, 27
- Binney J., 2012, *MNRAS*, **426**, 1324
- Bovy J., 2015, *ApJS*, **216**, 29
- Bovy J., Rix H.-W., Hogg D. W., 2012, *ApJ*, **751**, 131
- Carney B. W., Latham D. W., Laird J. B., Aguilar L. A., 1994, *AJ*, **107**, 2240
- Carollo D., et al., 2010, *ApJ*, **712**, 692
- Carollo D., et al., 2016, *Nature Physics*, **12**, 1170
- Casagrande L., VandenBerg D. A., 2018, *MNRAS*, **479**, L102
- Chené A.-N., 2017, in American Astronomical Society Meeting Abstracts. p. 236.08
- Chene A.-N., et al., 2014, in Advances in Optical and Mechanical Technologies for Telescopes and Instrumentation. p. 915147 ([arXiv:1409.7448](https://arxiv.org/abs/1409.7448)), [doi:10.1117/12.2057417](https://doi.org/10.1117/12.2057417)
- Chiba M., Beers T. C., 2000, *AJ*, **119**, 2843
- Cohen J. G., Kirby E. N., 2012, *ApJ*, **760**, 86
- Cutri R. M., et al., 2003, VizieR Online Data Catalog, *p. II/246*
- Di Matteo P., Haywood M., Lehnert M. D., Katz D., Khoperskov S., Snaith O. N., Gómez A., Robichon N., 2018, arXiv e-prints, *p. arXiv:1812.08232*
- Dotter A., Chaboyer B., Jevremović D., Kostov V., Baron E., Ferguson J. W., 2008, *ApJS*, **178**, 89
- Eilers A.-C., Hogg D. W., Rix H.-W., Ness M. K., 2019, *ApJ*, **871**, 120
- Fernández-Alvar E., et al., 2015, *A&A*, **577**, A81
- Fernández-Alvar E., et al., 2017, *MNRAS*, **465**, 1586
- Fernández-Alvar E., et al., 2018, *ApJ*, **852**, 50
- Fulbright J. P., 2002, *AJ*, **123**, 404
- Gaia Collaboration et al., 2016, *A&A*, **595**, A2
- Gaia Collaboration et al., 2018, *A&A*, **616**, A1
- Giclas H. L., Burnham R., Thomas N. G., 1971, Lowell proper motion survey Northern Hemisphere. The G numbered stars. 8991 stars fainter than magnitude 8 with motions > 0".26/year
- Giclas H. L., Burnham Jr. R., Thomas N. G., 1978, Lowell Observatory Bulletin, **8**, 89
- Gilmore G., Wyse R. F. G., 1985, *AJ*, **90**, 2015
- Gravity Collaboration et al., 2018, *A&A*, **615**, L15
- Green G. M., Schlafly E. F., Zucker C., Speagle J. S., Finkbeiner D. P., 2019, arXiv e-prints, *p. arXiv:1905.02734*
- Grevesse N., Anders E., 1989, in Waddington C. J., ed., American Institute of Physics Conference Series Vol. 183, Cosmic Abundances of Matter. pp 1–8, [doi:10.1063/1.38013](https://doi.org/10.1063/1.38013)
- Gustafsson B., Edvardsson B., Eriksson K., Mizuno-Wiedner M., Jørgensen U. G., Plez B., 2003, in Hubeny I., Mihalas D., Werner K., eds, Astronomical Society of the Pacific Conference Series Vol. 288, Stellar Atmosphere Modeling. p. 331
- Gustafsson B., Edvardsson B., Eriksson K., Jørgensen U. G., Nordlund Å., Plez B., 2008, *A&A*, **486**, 951
- Hawkins K., Jofré P., Masseron T., Gilmore G., 2015, *MNRAS*, **453**, 758
- Hayes C. R., et al., 2018, *ApJ*, **852**, 49
- Haywood M., Di Matteo P., Lehnert M. D., Snaith O., Khoperskov S., Gómez A., 2018, *ApJ*, **863**, 113
- Helmi A., Babusiaux C., Koppelman H. H., Massari D., Veljanoski J., Brown A. G. A., 2018, *Nature*, **563**, 85
- Hill V., et al., 2019, *A&A*, **626**, A15
- Ivans I. L., Sneden C., James C. R., Preston G. W., Fulbright J. P., Höflich P. A., Carney B. W., Wheeler J. C., 2003, *ApJ*, **592**, 906
- Jablonka P., et al., 2015, *A&A*, **583**, A67
- Jones E., Oliphant T., Peterson P., et al., 2001–, SciPy: Open source scientific tools for Python, <http://www.scipy.org/>
- Kordopatis G., et al., 2013, *MNRAS*, **436**, 3231
- Kurucz R. L., 2005, Memorie della Societa Astronomica Italiana Supplementi, **8**, 14
- Lind K., Bergemann M., Asplund M., 2012, *MNRAS*, **427**, 50
- Mackereth J. T., Bovy J., 2018, *PASP*, **130**, 114501
- Majewski S. R., et al., 2017, *AJ*, **154**, 94
- Manset N., Donati J. D., 2003, in SPIE Astronomical Telescopes + Instrumentation.
- Matsuno T., Aoki W., Suda T., 2019, *ApJ*, **874**, L35
- Matteucci F., 2003, *Ap&SS*, **284**, 539
- Matteucci F., Brocato E., 1990, *ApJ*, **365**, 539
- McMillan P. J., 2017, *MNRAS*, **465**, 76
- McWilliam A., Wallerstein G., Mottini M., 2013, *ApJ*, **778**, 149

Meléndez J., Ramírez I., 2004, *ApJ*, **615**, L33
 Monet D. G., et al., 2003, *AJ*, **125**, 984
 Myeong G. C., Evans N. W., Belokurov V., Sanders J. L., Koposov S. E., 2018a, *ApJ*, **856**, L26
 Myeong G. C., Evans N. W., Belokurov V., Sanders J. L., Koposov S. E., 2018b, *ApJ*, **863**, L28
 Myeong G. C., Vasiliev E., Iorio G., Evans N. W., Belokurov V., 2019, arXiv e-prints,
 Navarro J. F., Abadi M. G., Venn K. A., Freeman K. C., Anguiano B., 2011, *MNRAS*, **412**, 1203
 Nissen P. E., Schuster W. J., 2010, *A&A*, **511**, L10
 Nissen P. E., Schuster W. J., 2011, *A&A*, **530**, A15
 Norris J. E., Yong D., Venn K. A., Gilmore G., Casagrande L., Dotter A., 2017, *ApJS*, **230**, 28
 Reid M. J., Brunthaler A., 2004, *ApJ*, **616**, 872
 Schlafly E. F., Finkbeiner D. P., 2011, *ApJ*, **737**, 103
 Schönrich R., Binney J., Dehnen W., 2010, *MNRAS*, **403**, 1829
 Sestito F., et al., 2019, *MNRAS*, **484**, 2166
 Sitnova T., et al., 2015, *ApJ*, **808**, 148
 Skúladóttir Á., Tolstoy E., Salvadori S., Hill V., Pettini M., 2017, *A&A*, **606**, A71
 Sneden C., 1973, *ApJ*, **184**, 839
 Spite F., Spite M., 1982a, *A&A*, **115**, 357
 Spite M., Spite F., 1982b, *Nature*, **297**, 483
 Stephens A., Boesgaard A. M., 2002, *AJ*, **123**, 1647
 Stetson P. B., Pancino E., 2008, *PASP*, **120**, 1332
 The Astropy Collaboration et al., 2018, *AJ*, **156**, 123
 Tinsley B. M., 1979, *ApJ*, **229**, 1046
 Tolstoy E., Venn K. A., Shetrone M., Primas F., Hill V., Kaufer A., Szeifert T., 2003, *AJ*, **125**, 707
 Tolstoy E., Hill V., Tosi M., 2009, *ARA&A*, **47**, 371
 Venn K. A., Irwin M., Shetrone M. D., Tout C. A., Hill V., Tolstoy E., 2004, *AJ*, **128**, 1177
 Venn K. A., et al., 2012, *ApJ*, **751**, 102
 Venn K. A., Starkenburg E., Malo L., Martin N., Laevens B. P. M., 2017, *MNRAS*, **466**, 3741
 Vogt S. S., et al., 1994, in Crawford D. L., Craine E. R., eds, *Proc. SPIE Vol. 2198, Instrumentation in Astronomy VIII*. p. 362, doi:10.1117/12.176725
 Yong D., et al., 2013, *ApJ*, **762**, 26

APPENDIX A: SPECTRAL ANALYSIS METHODOLOGY

A1 Colour temperatures and physical gravities

Physical gravities and colour temperatures are determined simultaneously, using a Monte Carlo (MC) exploration of the Gaia DR2 stellar magnitudes and parallaxes, coupled with DSED (Dotter et al. 2008) isochrones. This method is entirely independent of spectroscopic methods, other than the initial assumption of the metallicity and $[\alpha/\text{Fe}]$ to create the stellar isochrones. We also have to assume that outer halo stars have old ages and low masses (we assume 12 Gyr (Carollo et al. 2016) and $0.8 M_{\text{sun}}$). Isochrones were constructed using both the Gaia DR2 and 2MASS (Cutri et al. 2003) filters to create G vs $BP - RP$ and J vs $J - K_s$ CMDs from which to map stellar parameters onto our stars.

For the MC estimates, we randomly sample the apparent G , $BP - RP$, J and $J - K_s$ magnitudes, value of $E(B - V)$, and parallax (ϖ) within their symmetric error distributions. Reddening corrections are determined using the geometric distances based on Gaia DR2 parallaxes Bailer-Jones et al. (2018), and the Bayestar17 reddening map from Green et al. (2019). Corrections for $E(B - V)$ were applied to the Gaia and

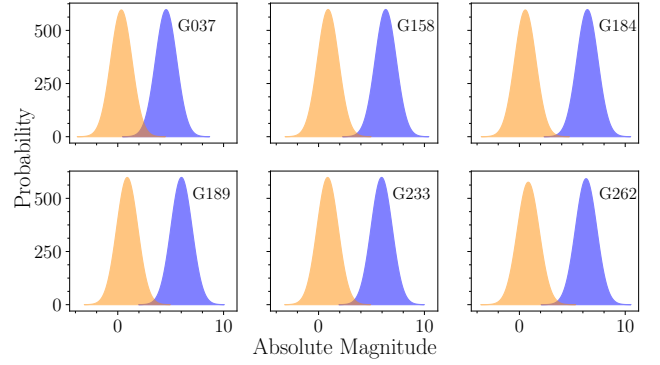


Figure A1. The resulting probability density distributions of absolute G and $BP - RP$ magnitudes for each star following 1500 realizations exploring photometric, reddening and parallax errors. The blue distribution shows the spread in the absolute Gaia G band magnitude, while the orange distribution shows the spread in absolute Gaia $BP - RP$ magnitude.

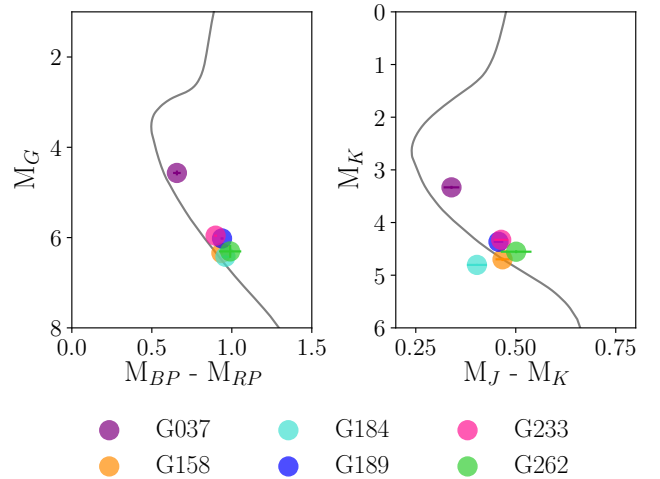


Figure A2. Optical and near-IR CMDs of the six stars under study following an MC analysis of their Gaia and 2MASS magnitudes, distances and reddening values. The underlying isochrone is a 12 Gyr DSED isochrone with metallicity $[\text{Fe}/\text{H}] = -2$ and an alpha enrichment of $+0.2$ dex.

2MASS filters using the coefficients from Green et al. (2019) and Casagrande & Vandenberg (2018), shown in Table A2. In the case of non-symmetric error distributions, we assume the larger error value to create a symmetric distribution. After 1500 realizations, the peak and spread in the probability density distributions were used to place each star on the G vs $BP - RP$ and the J vs $J - K_s$ CMDs, as shown in Fig. A1. Simultaneous fitting is performed in both colours to mitigate the effects of uncertainties in the reddening corrections.

The closest points on the isochrones were then mapped for each star in G , $BP - RP$, J and $J - K_s$ to determine the physical gravities and colour temperatures. These results are shown in Fig. A2. To validate these stellar parameters and account for uncertainties in the underlying isochrone physics, we also varied the isochrone ages by ± 2 Gyr, alpha abundances by ± 0.2 dex, and iron abundance by ± 0.15

Table A1. Photometric and distance information for each star. This includes the Gaia DR2 G -band photometry and $BP - RP$ colours, and the 2MASS $J - K_s$ colours (Cutri et al. 2003). Geometric distances are from Gaia DR2 parallaxes, and Bayesian corrected distances are from Bailer-Jones et al. (2018). The reddening $E(B-V)$ are from the Bayestar19 reddening map (Green et al. 2019) assuming the geometric distance and the conversion $E(B-V) = 0.981 \times (\text{Bayestar19})$ from Schlafly & Finkbeiner (2011).

Star	G mag	$BP - RP$ mag	$J - K_s$ mag	GDR2 Dist. (pc)	Geo. Dist. (pc)	$E(B-V)$
G037-037	12.13	0.76	0.381 ± 0.03	295.34 ± 6.05	$293.01^{+6.13}_{-5.88}$	$0.11^{+0.02}_{-0.03}$
G158-100	14.69	0.95	0.484 ± 0.04	461.43 ± 10.5	$455.53^{+4.62}_{-15.97}$	$0.01^{+0.02}_{-0.01}$
G184-007	14.19	1.09	0.453 ± 0.04	315.37 ± 1.87	$312.53^{+1.86}_{-1.84}$	$0.10^{+0.01}_{-0.03}$
G189-050	12.49	0.95	0.462 ± 0.02	194.02 ± 1.54	$192.95^{+1.55}_{-1.52}$	$0.00^{+0.02}_{-0.00}$
G233-026	11.68	0.91	0.466 ± 0.03	137.84 ± 0.46	137.30 ± 0.46	$0.00^{+0.01}_{-0.00}$
G262-021	13.58	1.04	0.521 ± 0.05	271.78 ± 0.96	269.66 ± 0.95	$0.04^{+0.11}_{-0.02}$

Table A2. Reddening coefficients used during the investigation of $\log g$ as described in Section A1 and applied as follows: $m_{\xi,0} = m_{\xi} - R_{\xi} E(B-V)$ where the value $E(B-V)$ is discussed in Section A1 and the reddening coefficient R_{ξ} for each filter ξ are the tabulated values.

Bands	Coefficients R_{ξ}	Source
(J, K_s)	(0.793, 0.303)	(Green et al. 2019)
(G_{BP}, G_{RP})	(3.374, 2.035)	(Casagrande & VandenBerg 2018)

dex (which is $\sim 1\sigma(\text{FeI}_{\text{NLTE}})$). This analysis proved that the largest uncertainties in the physical gravities and colour temperatures of these stars was due to our assumption of age. We adopt the uncertainty associated with the assumption of age as the uncertainties in our physical stellar parameters; in fact, these uncertainties are very similar to the sum of all of the errors when added in quadrature since the remaining uncertainties are small.

A2 Spectroscopic analysis

A2.1 Line Lists and Equivalent Widths

All spectra were radial velocity corrected using the IRAF task `fxcorr` using a template synthetic spectrum with similar atmospheric parameters. All spectra were also continuum normalized using a k-sigma clipping algorithm (e.g., Venn et al. (2012)), therefore the continuum fitting and radial velocity corrections available in DAOSpec were not enabled.

Initial equivalent width (EW) measurements were made using DAOSpec (Stetson & Pancino 2008), which finds and fits a Gaussian function to each line in a spectrum for a given line list. EW measurements were also made by hand for ~ 100 spectral lines ranging from 5-160 mÅ using the IRAF task `splot`. The results of this comparison are shown in Figure A3. Good fidelity was demonstrated in the EW regime from 10 to 150 mÅ. Deviations in the stronger lines are due to their non-Gaussian profiles (Lorentz wings), but we choose not to include strong lines which are more dependent on precision microturbulence values. In some cases, individual lines with $\text{EW} \leq 10$ mÅ were examined and added to the line list dependent on the local SNR in the wavelength region. Line measurements were taken when the local SNR ≥ 30 .

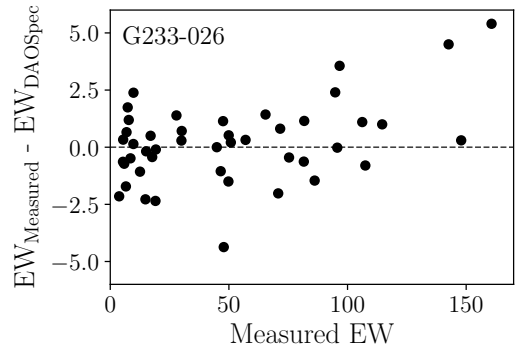


Figure A3. Results from an exploration of the fidelity of DAOSpec EW line measurements as described in Section A2.1 for the star G233-026.

The lowest EWs are taken as 5 mÅ in the best SNR regions (≥ 100).

A2.2 Spectroscopic stellar parameters

Although we chose to adopt the stellar parameters associated with isochrone-mapping technique described in Section A1, we also derived the stellar parameters spectroscopically to compare the two techniques. This was done through an iterative optimization technique using the LTE line analysis code MOOG (Snedden 1973). A temperature range of ± 500 K and $\log g$ of ± 0.5 (units of cm/s^2) were examined around the initial SB02 stellar parameters, in units of ± 100 K and ± 0.1 , respectively. Minimization of $\log(\text{Fe I})$ vs. excitation potential was used to derive the spectroscopic effective temperature (T_{eff}), and minimization of $\log(\text{Fe I})$ vs. $\log(\text{EW}/\text{wavelength})$ was used to determine a microturbulence (ξ) value. Ionization equilibrium between the $\log(\text{Fe I})$ and $\log(\text{Fe II})$ abundances was used to constrain a spectroscopic gravity. Several iterations of this minimization process were undertaken to avoid a local minimum in parameter space. The final spectroscopic parameters are shown in Table 3.

A2.3 NLTE corrections

After adopting the isochrone-mapped stellar parameters we re-derived the metallicity using the 1D, LTE stellar analy-

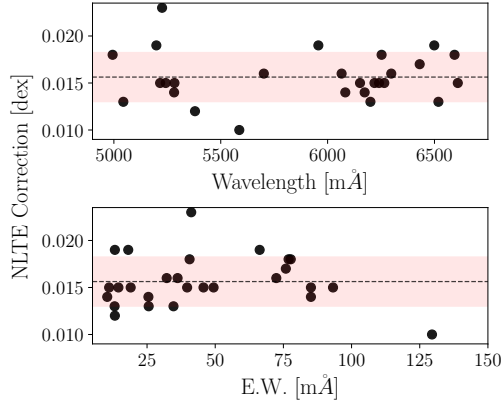


Figure A4. Non-LTE corrections for Fe I lines as a function of wavelength and E.W. measurement for G233-026. The mean non-LTE Fe I correction is shown as a dashed line, with the 1σ uncertainties in red.

sis code MOOG (Snedden 1973). Following this, we investigated the impact of non-LTE corrections for Fe I lines using the individual spectral line corrections listed in INSPECT⁶ (Bergemann et al. 2012; Lind et al. 2012). The NLTE corrections are similar for all available lines regardless of EW or χ value, per star, thus we calculated a simple mean offset to the Fe I LTE abundances. Furthermore, the non-LTE corrections are generally small (e.g., see Fig. A4, having very little impact on our results. NLTE-corrected metallicities are listed in Table 3 as bolded values.

A3 Summary

In summary, we find general agreement between our spectroscopic and physical stellar parameters, as in Table 3. We also tabulate the Gaia DR2 Apsis values for T_{eff} , however we did not use the Apsis values which assume a constant $E(B-V)=0.307$ (Andrae et al. 2018). Both the spectroscopic and colour temperatures have systematically lower errors than Apsis, which predicts an RMS error of 324 K. Also the spectroscopic gravities (ours and those of SB02) tend to be systematically lower than the physical gravities. Similar results were found by Sestito et al. (2019) in their analysis of the ultra metal-poor stars from Gaia DR2 data.

For the remainder of this analysis the physical gravities and colour temperatures are adopted for each star. The microturbulence values are determined using the formula for metal-poor F and G dwarfs by Sitnova et al. (2015), which is calibrated on more stars with more spectral lines in a homogeneous NLTE analysis. The final parameters are noted in bold for each star in Table 3.

A4 A brief look at odd-Z elements and Barium

In Fig. A5, we show the abundances for a select set of elements, the odd-Z element Mn, the even-Z element Zn and the heavy element Ba. The *Gaia*-Enceladus and *Gaia*-Sequoia classified stars are plotted as separate populations

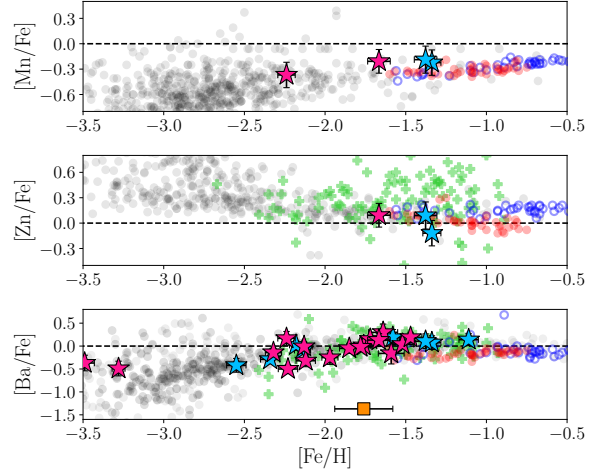


Figure A5. Select abundances for the odd-Z element Mn, the even-Z element Zn and the heavy element Ba. Literature data (black dots, red and blue circles) follows the convention of Fig. 5. Stars identified as being part of the *Gaia*-Sequoia accretion event are shown as pink stars, stars associated with the *Gaia*-Enceladus accretion event are shown in sky blue. The chemically distinct star G251-024 (discussed in Section 4.3.1) is shown as the orange box in the final plot of [Ba/Fe]. Data from the Sculptor dGal is also shown for Zn (Skúladóttir et al. 2017; Hill et al. 2019) and Ba (Hill et al. 2019).

in these plots (sky blue and pink stars respectively), alongside our re-analyzed stars that were not associated with either accretion event. We also highlight the Ba abundance of the chemically interesting star G251-024 discussed in Section 4.3.1. Unfortunately as SB02 did not look at Mn or Zn, our interpretation of these elements is limited to our re-analysed sample. Comparing with the halo stars, none of the stars in our subsample appear unique in Mn or Zn, with the exception of the low Zn, *Gaia*-Enceladus classified star, G233-026. This may be interesting to examine in the future when more chemistry is obtained for potential *Gaia*-Enceladus and *Gaia*-Sequoia stars. Comparing the Zn and Ba abundances against the Sculptor data of Skúladóttir et al. (2017) and Hill et al. (2019), none of the stars show the same level of Zn-enhancement seen in Sculptor.

APPENDIX B: MORE ON ORBITS

As discussed in Section 4, orbits were determined for all the stars in the SB02 sample. In Fig. B1 we show orbits for four of the stars in our sub-sample (G262-021, G184-007, G233-026 and G158-100) to demonstrate their orbital diversity. An additional two orbits of chemodynamically interesting stars are also shown, the metal-poor *Gaia*-Sequoia associated star G082-023 and G122-051, the potential MWTD star. The astrometric parameters of the entire SB02 sample are listed in Table B1, resultant orbital parameters are listed in Tables B2 and B3.

APPENDIX C: TABLES OF ABUNDANCES AND EQUIVALENT WIDTHS

⁶ Data obtained from the INSPECT database, version 1.0 (www.inspect-stars.net)

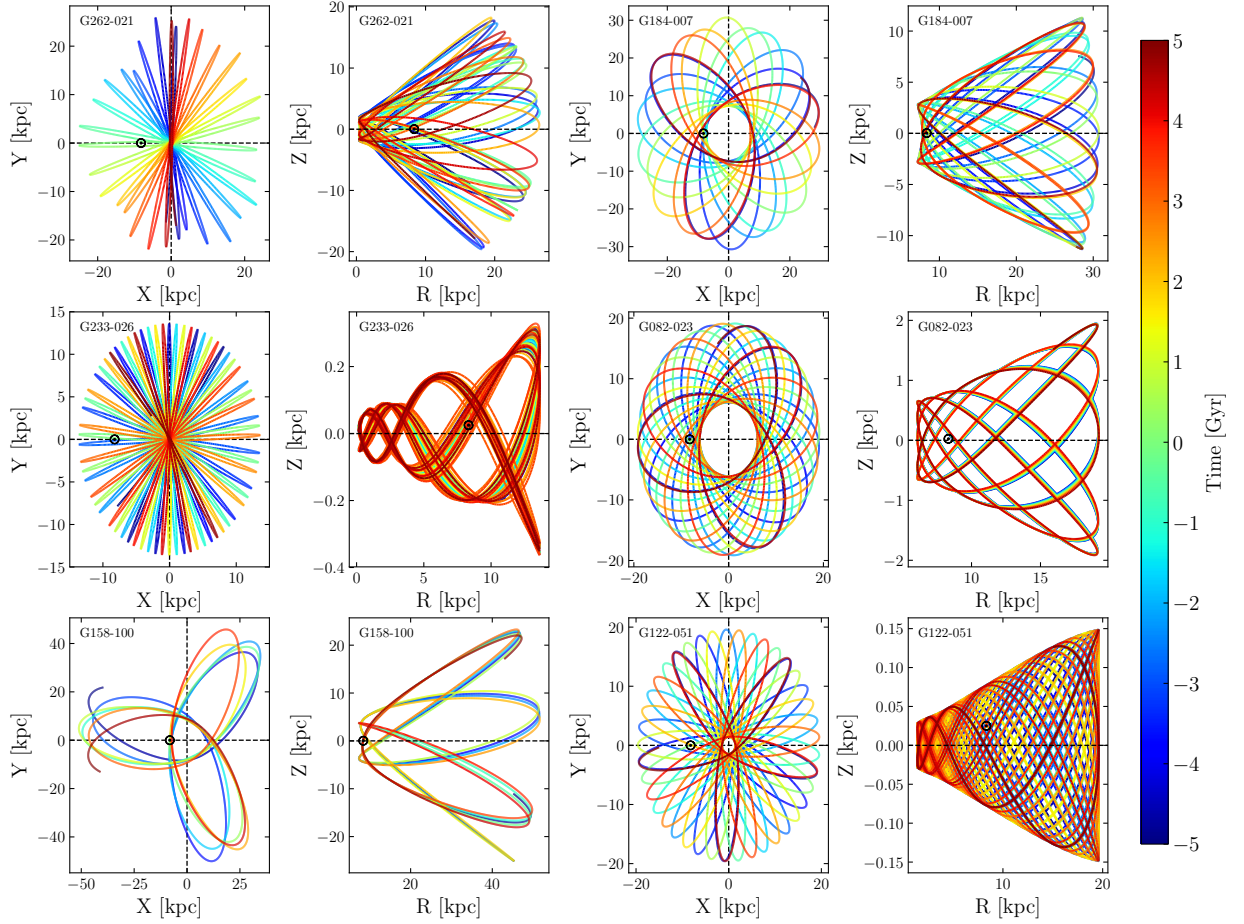


Figure B1. Orbits of four stars in our subset (G262-021, G184-007, G233-026 and G158-100) are shown following integration both forwards and backwards in time for 5 Gyr in a [McMillan \(2017\)](#) potential. The first and third columns show galactocentric X and Y , and the second and fourth columns show galactocentric cylindrical radius, R and height above the galactic plane, Z . The dashed lines mark the zero point of each coordinate, and the black symbol marks the location of the sun.

Table B1. Basic astrometric parameters from *Gaia* and radial velocities from this work and SB02. The first section shows MV19 stars spectroscopically studied in this work with updated radial velocities determined in this work. The remaining radial velocities are from SB02.

Name	α [deg]	δ [deg]	π [mas]	μ_α [mas/yr]	μ_δ [mas/yr]	RV [km/s]
G037-037	50.91 ± 0.06	33.97 ± 0.03	3.39 ± 0.07	-72.95 ± 0.09	-359.86 ± 0.07	-143.0 ± 0.4
G158-100	8.48 ± 0.04	-12.13 ± 0.03	2.17 ± 0.05	157.6 ± 0.1	-191.43 ± 0.09	-360.6 ± 1.1
G184-007	276.05 ± 0.01	27.29 ± 0.02	3.17 ± 0.02	-272.86 ± 0.02	-169.26 ± 0.03	-370.6 ± 0.5
G189-050	344.11 ± 0.03	33.88 ± 0.03	5.15 ± 0.04	-98.77 ± 0.07	-371.24 ± 0.05	-320.9 ± 0.6
G233-026	339.98 ± 0.02	61.72 ± 0.02	7.25 ± 0.02	-167.54 ± 0.05	-106.58 ± 0.04	-313.6 ± 0.6
G262-021	308.86 ± 0.01	64.9 ± 0.01	3.68 ± 0.01	214.19 ± 0.03	207.98 ± 0.03	-214.0 ± 0.5
G031-026	2.08 ± 0.04	-5.25 ± 0.02	5.19 ± 0.05	352.97 ± 0.08	-131.16 ± 0.04	-215.6 ± 0.7
G171-050	5.02 ± 0.03	42.73 ± 0.01	2.56 ± 0.03	183.46 ± 0.04	-172.39 ± 0.02	-191.4 ± 0.5
G033-031	15.35 ± 0.08	15.25 ± 0.04	6.36 ± 0.08	324.75 ± 0.15	37.46 ± 0.09	255.6 ± 0.6
G005-019	47.86 ± 0.04	12.62 ± 0.03	6.19 ± 0.04	-24.81 ± 0.08	-467.59 ± 0.07	-215.6 ± 0.6
G005-035	51.21 ± 0.05	12.25 ± 0.03	9.27 ± 0.05	567.79 ± 0.1	-491.78 ± 0.07	87.5 ± 0.7
G246-038	52.84 ± 0.02	66.73 ± 0.02	20.16 ± 0.03	1191.57 ± 0.03	-1066.35 ± 0.05	-160.6 ± 0.5
G095-060	59.01 ± 0.02	41.99 ± 0.01	3.62 ± 0.03	112.26 ± 0.05	-236.62 ± 0.04	91.8 ± 0.7
G082-005	63.74 ± 0.03	-5.63 ± 0.02	11.49 ± 0.04	636.59 ± 0.05	188.57 ± 0.03	296.5 ± 0.6
G082-023	67.56 ± 0.03	-3.05 ± 0.02	2.42 ± 0.03	117.11 ± 0.05	-243.86 ± 0.04	26.9 ± 0.5
G247-027	69.3 ± 0.02	60.74 ± 0.01	4.16 ± 0.02	198.29 ± 0.03	-247.68 ± 0.03	-156.1 ± 0.9
G084-052	81.36 ± 0.02	-2.32 ± 0.02	2.98 ± 0.03	91.71 ± 0.05	-165.66 ± 0.05	214.1 ± 1.1
G097-040	81.68 ± 0.02	9.82 ± 0.02	2.61 ± 0.03	122.34 ± 0.04	-165.56 ± 0.03	2.2 ± 0.7
LTT-2415	89.1 ± 0.02	-27.86 ± 0.02	2.55 ± 0.02	236.47 ± 0.03	-157.22 ± 0.04	253.6 ± 0.7
G110-034	106.44 ± 0.04	11.31 ± 0.03	3.5 ± 0.04	-29.02 ± 0.07	-189.88 ± 0.06	27.2 ± 0.9
G088-032	112.67 ± 0.04	24.09 ± 0.04	3.88 ± 0.05	162.26 ± 0.09	-233.31 ± 0.07	-237.7 ± 0.6
G088-042	113.98 ± 0.03	19.2 ± 0.03	2.32 ± 0.04	92.05 ± 0.06	-197.85 ± 0.05	391.7 ± 0.5
G251-024	106.73 ± 0.03	72.31 ± 0.05	30.51 ± 0.06	-41.61 ± 0.07	-240.26 ± 0.09	6.2 ± 0.8
G046-005	132.62 ± 0.03	7.62 ± 0.03	11.73 ± 0.04	252.69 ± 0.07	-580.74 ± 0.05	292.9 ± 0.5
G009-036	134.5 ± 0.1	24.47 ± 0.05	4.58 ± 0.08	201.56 ± 0.17	-240.4 ± 0.12	-48.5 ± 0.7
G114-042	137.69 ± 0.03	-3.8 ± 0.03	3.15 ± 0.04	130.36 ± 0.07	-256.38 ± 0.06	-86.8 ± 0.6
G116-053	146.93 ± 0.05	33.38 ± 0.04	3.04 ± 0.08	191.43 ± 0.11	-165.8 ± 0.08	-112.4 ± 1.7
G121-012	176.15 ± 0.05	25.54 ± 0.05	6.93 ± 0.09	-518.65 ± 0.09	-44.82 ± 0.11	198.3 ± 0.5
G197-030	176.77 ± 0.01	59.99 ± 0.01	4.69 ± 0.02	-412.82 ± 0.03	-94.24 ± 0.03	137.3 ± 0.7
G122-051	178.27 ± 0.05	37.69 ± 0.03	108.96 ± 0.05	4002.57 ± 0.07	-5817.86 ± 0.06	-98.3 ± 0.3
G011-044	182.73 ± 0.2	0.4 ± 0.12	5.81 ± 0.27	-54.08 ± 0.64	-435.69 ± 0.13	99.0 ± 0.8
G238-030	199.41 ± 0.02	64.25 ± 0.02	3.09 ± 0.02	-283.94 ± 0.04	-156.05 ± 0.04	226.4 ± 0.4
G064-012	205.01 ± 0.06	-0.04 ± 0.05	3.76 ± 0.09	-228.84 ± 0.13	-80.07 ± 0.13	442.6 ± 0.7
G165-039	209.79 ± 0.02	33.86 ± 0.02	5.72 ± 0.03	89.64 ± 0.03	-427.29 ± 0.04	-170.6 ± 0.7
G064-037	210.63 ± 0.05	-5.65 ± 0.08	4.21 ± 0.1	-54.71 ± 0.18	-396.02 ± 0.25	82.0 ± 0.7
G166-037	218.71 ± 0.02	25.17 ± 0.03	5.12 ± 0.03	-45.65 ± 0.06	-342.53 ± 0.06	368.4 ± 0.7
G201-005	219.04 ± 0.02	55.55 ± 0.02	4.24 ± 0.02	122.64 ± 0.04	-295.7 ± 0.05	-34.7 ± 0.7
G239-026	221.17 ± 0.02	71.45 ± 0.02	4.04 ± 0.02	19.02 ± 0.05	-301.9 ± 0.04	-287.8 ± 0.8
G015-013	228.13 ± 0.03	6.03 ± 0.03	7.67 ± 0.04	-439.52 ± 0.06	-659.07 ± 0.07	219.7 ± 0.5
G016-025	240.34 ± 0.02	5.39 ± 0.01	3.38 ± 0.02	-329.67 ± 0.03	-290.64 ± 0.03	23.8 ± 0.6
G180-024	240.8 ± 0.02	42.24 ± 0.03	8.48 ± 0.03	-195.75 ± 0.04	-365.08 ± 0.05	-150.8 ± 0.6
G168-042B	244.97 ± 0.54	22.64 ± 0.62	13.93 ± 0.74	-46.29 ± 1.07	-452.7 ± 1.14	157.9 ± 0.6
G170-021	257.31 ± 0.04	22.74 ± 0.07	4.2 ± 0.08	-181.56 ± 0.1	-192.49 ± 0.14	-222.0 ± 0.9
G020-008	264.94 ± 0.04	2.42 ± 0.04	9.84 ± 0.05	-366.01 ± 0.07	75.12 ± 0.07	-397.0 ± 0.6
G144-028	310.6 ± 0.03	11.29 ± 0.02	4.26 ± 0.03	-106.25 ± 0.05	-349.11 ± 0.04	-13.2 ± 0.7
G025-024	319.17 ± 0.04	-1.3 ± 0.03	5.52 ± 0.05	266.37 ± 0.07	-248.85 ± 0.06	44.6 ± 0.4
G093-001	319.63 ± 0.03	2.61 ± 0.02	1.85 ± 0.03	-24.71 ± 0.05	-195.51 ± 0.04	-119.4 ± 0.6
G026-012	323.4 ± 0.04	0.4 ± 0.04	3.44 ± 0.05	245.26 ± 0.08	-28.87 ± 0.08	-238.3 ± 0.5
G188-020	325.54 ± 0.03	31.0 ± 0.04	2.76 ± 0.06	-128.3 ± 0.08	-260.08 ± 0.08	-114.9 ± 0.7
G188-030	328.82 ± 0.02	32.65 ± 0.02	12.34 ± 0.03	760.81 ± 0.04	124.75 ± 0.06	-184.9 ± 0.5

Table B2. Orbital properties for the SB02 stars. The first section shows MV19 stars spectroscopically studied in this work. Errors were determined via 100 MC realizations exploring the errors associated with the input Gaia parameters.

Name	R_{peri} [kpc]	R_{apo} [kpc]	T_{rad} [Myr]	U [km/s]	V [km/s]	W [km/s]
G037-037	7.09 ± 0.08	58.12 ± 5.67	727.6 ± 71.5	187.5 ± 1.11	-392.11 ± 8.97	-298.31 ± 5.12
G158-100	8.233 ± 0.001	51.86 ± 5.7	653.5 ± 70.1	-42.03 ± 2.25	222.29 ± 3.32	-600.88 ± 13.62
G184-007	7.7 ± 0.01	30.58 ± 0.75	396.4 ± 8.4	78.06 ± 1.69	165.24 ± 1.72	-569.44 ± 1.77
G189-050	2.1 ± 0.01	24.09 ± 0.39	278.7 ± 4.6	298.19 ± 1.83	-105.56 ± 1.87	-351.76 ± 0.71
G233-026	0.13 ± 0.01	13.63 ± 0.03	146.6 ± 0.3	230.93 ± 0.48	-15.79 ± 0.04	-245.18 ± 0.6
G262-021	0.23 ± 0.01	26.72 ± 0.31	302.9 ± 3.6	-328.81 ± 1.46	-119.68 ± 0.31	-237.36 ± 0.48
G031-026	1.93 ± 0.06	13.36 ± 0.16	158.6 ± 2.0	-202.22 ± 2.37	105.6 ± 1.26	-319.32 ± 2.68
G171-050	7.19 ± 0.03	20.5 ± 1.02	284.3 ± 11.5	-117.44 ± 2.52	-268.17 ± 4.16	-391.52 ± 3.04
G033-031	4.96 ± 0.05	52.83 ± 0.49	638.5 ± 5.9	-302.83 ± 2.9	-152.9 ± 0.59	32.98 ± 1.6
G005-019	0.62 ± 0.03	21.76 ± 0.19	244.2 ± 2.5	303.79 ± 0.97	-87.25 ± 1.7	-271.6 ± 1.74
G005-035	2.73 ± 0.06	10.03 ± 0.04	122.2 ± 0.8	-124.66 ± 0.72	-32.68 ± 0.46	-355.5 ± 2.23
G246-038	3.16 ± 0.01	10.24 ± 0.02	128.8 ± 0.2	-126.84 ± 0.5	-58.64 ± 0.09	-366.87 ± 0.46
G095-060	0.31 ± 0.05	12.95 ± 0.07	150.1 ± 1.0	-180.68 ± 0.87	-145.25 ± 0.91	-245.13 ± 1.96
G082-005	0.9 ± 0.01	27.59 ± 0.13	308.7 ± 1.5	-345.21 ± 0.67	40.78 ± 0.86	-174.22 ± 0.44
G082-023	6.08 ± 0.08	19.18 ± 0.78	251.9 ± 9.3	176.18 ± 2.27	-45.07 ± 0.49	-488.32 ± 5.44
G247-027	3.63 ± 0.06	8.78 ± 0.02	116.1 ± 0.6	-56.63 ± 1.29	-33.66 ± 0.19	-373.49 ± 1.76
G084-052	2.84 ± 0.11	8.77 ± 0.01	111.8 ± 0.7	-45.54 ± 1.73	-62.15 ± 0.38	-346.42 ± 3.15
G097-040	2.86 ± 0.12	9.5 ± 0.04	117.9 ± 1.3	91.79 ± 1.05	39.52 ± 0.35	-351.64 ± 3.9
LTT-2415	7.6 ± 0.01	31.67 ± 1.38	408.8 ± 15.8	135.55 ± 2.3	197.15 ± 2.48	-528.05 ± 3.27
G110-034	0.77 ± 0.07	9.14 ± 0.04	110.4 ± 0.2	55.01 ± 1.09	-135.86 ± 1.86	-202.39 ± 2.5
G088-032	0.29 ± 0.06	25.98 ± 0.31	287.3 ± 3.7	339.78 ± 1.43	2.63 ± 0.93	-250.84 ± 4.31
G088-042	6.83 ± 0.11	32.34 ± 1.3	408.5 ± 15.9	-180.45 ± 2.69	142.68 ± 0.26	-532.19 ± 6.38
G251-024	7.29 ± 0.01	8.48 ± 0.02	146.4 ± 0.3	-19.02 ± 0.5	1.36 ± 0.33	-10.82 ± 0.38
G046-005	4.22 ± 0.03	8.6 ± 0.01	126.6 ± 0.2	-25.23 ± 0.6	139.87 ± 0.27	-351.77 ± 0.76
G009-036	0.2 ± 0.06	14.43 ± 0.22	160.3 ± 2.5	231.89 ± 2.95	80.28 ± 1.54	-219.19 ± 3.66
G114-042	0.37 ± 0.07	40.67 ± 1.59	463.2 ± 19.0	389.17 ± 4.85	-79.54 ± 0.7	-196.51 ± 4.12
G116-053	0.57 ± 0.11	31.59 ± 2.08	359.0 ± 24.4	351.92 ± 7.68	100.97 ± 5.49	-195.91 ± 6.49
G121-012	0.69 ± 0.04	26.38 ± 0.61	298.3 ± 6.7	-328.7 ± 3.86	106.75 ± 1.15	-191.06 ± 2.19
G197-030	0.61 ± 0.02	39.3 ± 0.45	446.4 ± 5.4	-387.62 ± 1.44	66.49 ± 0.56	-186.48 ± 0.94
G122-051	1.417 ± 0.002	19.61 ± 0.02	218.7 ± 0.2	291.56 ± 0.14	-6.34 ± 0.29	-146.51 ± 0.08
G011-044	1.88 ± 0.33	10.74 ± 0.37	126.5 ± 6.4	153.91 ± 6.05	-72.46 ± 7.0	-321.14 ± 12.05
G238-030	5.37 ± 0.01	81.99 ± 2.12	1027.3 ± 28.7	-280.69 ± 1.52	375.24 ± 1.23	-267.82 ± 2.76
G064-012	8.093 ± 0.002	43.6 ± 0.77	557.0 ± 9.1	24.27 ± 3.23	400.12 ± 0.62	-354.67 ± 4.73
G165-039	0.15 ± 0.02	20.49 ± 0.19	233.6 ± 2.2	279.85 ± 1.49	-142.48 ± 0.75	-242.99 ± 1.12
G064-037	3.46 ± 0.19	15.77 ± 0.67	197.0 ± 8.8	202.44 ± 2.87	-148.37 ± 4.31	-369.02 ± 6.95
G166-037	4.69 ± 0.02	83.45 ± 0.92	1042.7 ± 12.4	322.92 ± 1.18	339.09 ± 0.54	-163.15 ± 1.52
G201-005	2.54 ± 0.02	35.81 ± 0.54	414.0 ± 6.3	353.8 ± 1.97	56.91 ± 0.72	-84.99 ± 0.63
G239-026	0.57 ± 0.01	30.55 ± 0.33	341.3 ± 4.0	362.0 ± 1.32	13.01 ± 0.96	-280.36 ± 0.83
G015-013	5.11 ± 0.03	25.75 ± 0.29	320.5 ± 3.4	228.29 ± 0.43	162.32 ± 0.35	-452.87 ± 1.93
G016-025	7.75 ± 0.01	33.41 ± 1.54	429.0 ± 17.7	77.47 ± 0.6	163.79 ± 1.14	-581.63 ± 4.45
G180-024	0.16 ± 0.01	9.2 ± 0.01	98.9 ± 0.1	112.07 ± 0.45	-20.34 ± 0.59	-243.53 ± 0.55
G168-042B	4.77 ± 0.19	19.17 ± 0.11	241.3 ± 0.9	211.3 ± 6.06	93.26 ± 1.29	-17.89 ± 5.79
G170-021	2.99 ± 0.15	8.11 ± 0.01	103.7 ± 1.2	16.88 ± 2.88	-5.02 ± 2.08	-359.51 ± 4.85
G020-008	0.07 ± 0.01	27.63 ± 0.12	307.7 ± 1.4	-350.73 ± 0.52	56.84 ± 0.75	-226.17 ± 0.48
G144-028	0.04 ± 0.03	21.86 ± 0.41	245.3 ± 4.8	308.11 ± 2.6	-100.82 ± 0.99	-242.89 ± 1.92
G025-024	7.965 ± 0.004	13.46 ± 0.18	215.9 ± 2.0	-23.61 ± 0.59	-275.44 ± 2.06	-124.76 ± 1.43
G093-001	3.87 ± 0.09	23.11 ± 1.42	280.3 ± 16.7	250.07 ± 4.76	-127.2 ± 3.15	-428.89 ± 5.94
G026-012	0.42 ± 0.02	25.76 ± 0.85	289.7 ± 10.0	-330.42 ± 3.34	-101.64 ± 3.6	-197.42 ± 0.9
G188-020	0.58 ± 0.04	79.35 ± 9.89	960.8 ± 133.7	449.19 ± 9.9	-129.76 ± 3.69	-212.07 ± 2.87
G188-030	0.74 ± 0.01	16.65 ± 0.06	186.4 ± 0.7	-260.64 ± 0.58	-84.3 ± 0.34	-187.12 ± 0.45

Table B3. Additional kinematic parameters. The first section shows MV19 stars spectroscopically studied in this work. Errors were determined via 100 MC realizations exploring the errors associated with the input Gaia parameters.

Name	J_ϕ (L_z) [kpc km/s]	J_r [kpc km/s]	J_z [kpc km/s]	e	Z_{\max} [kpc]	E [km ² s ⁻²]
G037-037	-530.47 ± 43.09	3041.0 ± 400.58	2773.21 ± 50.35	0.78 ± 0.02	57.22 ± 5.5	-85411.3 ± 4019.1
G158-100	-3038.04 ± 113.08	2471.18 ± 409.74	485.35 ± 27.55	0.73 ± 0.03	24.18 ± 1.72	-89901.4 ± 4321.8
G184-007	-2684.13 ± 13.44	1074.79 ± 50.16	261.27 ± 4.92	0.6 ± 0.01	11.15 ± 0.34	-111490.3 ± 979.4
G189-050	-924.49 ± 5.35	1515.37 ± 28.66	140.06 ± 6.15	0.839 ± 0.002	7.6 ± 0.3	-126442.1 ± 776.8
G233-026	-69.42 ± 4.89	1172.94 ± 3.84	1.51 ± 0.01	0.981 ± 0.001	0.305 ± 0.001	-156530.1 ± 112.4
G262-021	-120.49 ± 4.11	2137.36 ± 23.83	210.23 ± 1.19	0.983 ± 0.001	11.16 ± 0.17	-122127.9 ± 550.6
G031-026	-724.49 ± 22.39	674.61 ± 6.45	159.63 ± 5.39	0.748 ± 0.004	4.9 ± 0.07	-153858.2 ± 629.2
G171-050	-1365.77 ± 27.15	466.79 ± 54.48	1124.05 ± 20.91	0.48 ± 0.02	16.53 ± 0.82	-127095.9 ± 1908.3
G033-031	2175.66 ± 13.66	3178.34 ± 49.53	235.76 ± 1.72	0.828 ± 0.003	19.0 ± 0.17	-90291.6 ± 380.0
G005-019	-312.88 ± 14.46	1678.21 ± 7.95	97.22 ± 4.84	0.945 ± 0.002	5.73 ± 0.22	-132173.1 ± 461.2
G005-035	-1017.16 ± 18.55	353.75 ± 6.28	7.29 ± 0.24	0.57 ± 0.01	0.57 ± 0.01	-167295.3 ± 346.3
G246-038	-1107.26 ± 3.79	311.93 ± 1.53	31.03 ± 0.12	0.528 ± 0.002	1.378 ± 0.004	-164744.2 ± 97.3
G095-060	-122.02 ± 16.78	822.4 ± 8.63	415.27 ± 7.38	0.95 ± 0.01	8.92 ± 0.12	-155122.1 ± 297.4
G082-005	494.85 ± 3.63	2162.38 ± 12.56	14.02 ± 0.69	0.937 ± 0.001	2.16 ± 0.07	-121091.9 ± 219.2
G082-023	-2198.98 ± 47.85	547.92 ± 39.28	21.03 ± 0.47	0.52 ± 0.01	1.83 ± 0.08	-132337.3 ± 1747.2
G247-027	-1187.94 ± 14.9	180.58 ± 4.62	8.77 ± 0.11	0.42 ± 0.01	0.562 ± 0.004	-170347.1 ± 278.4
G084-052	-956.63 ± 27.35	250.35 ± 11.53	38.82 ± 0.57	0.51 ± 0.01	1.4 ± 0.01	-172404.7 ± 309.4
G097-040	-1024.24 ± 34.14	301.85 ± 11.72	12.49 ± 0.25	0.54 ± 0.01	0.75 ± 0.01	-169342.4 ± 572.1
LTT-2415	-2523.85 ± 29.03	1151.86 ± 91.63	421.27 ± 8.6	0.61 ± 0.01	14.85 ± 0.7	-110076.8 ± 1762.3
G110-034	253.63 ± 21.22	440.64 ± 6.38	370.88 ± 18.12	0.84 ± 0.01	6.23 ± 0.21	-170773.2 ± 258.5
G088-032	-171.2 ± 36.83	2217.7 ± 12.89	0.72 ± 0.08	0.978 ± 0.005	0.38 ± 0.03	-124226.8 ± 580.0
G088-042	-2544.75 ± 56.59	1314.64 ± 73.78	209.99 ± 2.07	0.65 ± 0.01	10.71 ± 0.28	-109916.3 ± 1730.8
G251-024	1829.72 ± 3.16	7.42 ± 0.06	0.096 ± 0.005	0.0754 ± 0.0002	0.046 ± 0.001	-158648.1 ± 96.3
G046-005	-979.78 ± 6.33	102.79 ± 1.96	304.83 ± 1.48	0.341 ± 0.004	4.7 ± 0.02	-166166.9 ± 93.7
G009-036	101.52 ± 31.05	1153.89 ± 33.48	85.99 ± 4.45	0.97 ± 0.01	3.66 ± 0.16	-152378.5 ± 774.3
G114-042	218.47 ± 36.88	3391.54 ± 154.48	58.09 ± 1.02	0.982 ± 0.004	7.54 ± 0.35	-103012.2 ± 1776.8
G116-053	297.06 ± 55.07	2488.55 ± 192.86	169.21 ± 22.62	0.96 ± 0.01	11.36 ± 1.59	-114428.3 ± 3069.1
G121-012	353.54 ± 17.83	2035.57 ± 65.66	130.72 ± 4.09	0.949 ± 0.004	8.2 ± 0.08	-122883.0 ± 1056.8
G197-030	354.88 ± 7.99	3219.79 ± 41.47	34.82 ± 0.71	0.97 ± 0.001	5.32 ± 0.1	-104605.6 ± 525.2
G122-051	711.3 ± 0.66	1365.32 ± 1.59	0.26 ± 0.02	0.8652 ± 0.0002	0.17 ± 0.01	-137398.7 ± 37.1
G011-044	-733.73 ± 99.65	512.33 ± 26.16	52.01 ± 12.12	0.7 ± 0.03	2.02 ± 0.34	-165338.2 ± 2479.0
G238-030	-336.76 ± 23.71	5124.01 ± 154.93	2578.64 ± 9.86	0.877 ± 0.003	81.28 ± 2.0	-72507.6 ± 966.6
G064-012	-986.19 ± 37.83	1847.76 ± 53.48	2386.02 ± 26.1	0.687 ± 0.005	41.41 ± 0.59	-96571.1 ± 699.1
G165-039	-69.08 ± 9.05	1564.01 ± 11.88	302.7 ± 4.66	0.986 ± 0.002	10.96 ± 0.13	-134318.7 ± 439.5
G064-037	-1111.51 ± 56.2	610.62 ± 21.53	290.9 ± 16.04	0.64 ± 0.004	7.64 ± 0.46	-143708.3 ± 2112.4
G166-037	583.69 ± 12.28	5379.07 ± 67.12	2082.32 ± 9.71	0.893 ± 0.001	80.64 ± 0.91	-71923.6 ± 410.1
G201-005	1264.55 ± 4.65	2415.32 ± 45.93	39.04 ± 1.13	0.868 ± 0.002	5.06 ± 0.14	-108288.0 ± 672.9
G239-026	-330.09 ± 6.57	2520.84 ± 25.81	4.11 ± 0.31	0.9635 ± 0.0005	1.16 ± 0.06	-116432.7 ± 521.7
G015-013	-1783.76 ± 15.57	1090.56 ± 16.44	323.64 ± 2.46	0.668 ± 0.002	11.7 ± 0.09	-120782.0 ± 496.4
G016-025	-2780.17 ± 34.84	1258.42 ± 103.93	252.91 ± 1.98	0.62 ± 0.01	11.84 ± 0.51	-107921.1 ± 1868.4
G180-024	-77.26 ± 4.46	756.56 ± 2.09	3.01 ± 0.16	0.967 ± 0.002	0.32 ± 0.01	-177313.4 ± 45.4
G168-042B	1765.2 ± 47.21	700.79 ± 31.14	87.91 ± 2.05	0.6 ± 0.01	4.34 ± 0.05	-134044.6 ± 156.4
G170-021	-1017.1 ± 38.4	200.6 ± 14.5	1.15 ± 0.09	0.46 ± 0.02	0.17 ± 0.01	-176451.0 ± 624.4
G020-008	40.96 ± 3.97	2395.99 ± 11.34	26.45 ± 0.86	0.995 ± 0.0005	3.2 ± 0.07	-121137.2 ± 208.3
G144-028	-22.0 ± 14.75	1820.35 ± 26.61	129.37 ± 3.14	0.996 ± 0.002	6.89 ± 0.22	-131884.8 ± 913.8
G025-024	876.05 ± 11.82	87.88 ± 5.8	1371.18 ± 23.24	0.26 ± 0.01	12.21 ± 0.21	-140243.3 ± 431.6
G093-001	-1460.34 ± 42.84	1100.67 ± 90.35	211.12 ± 10.28	0.71 ± 0.01	8.77 ± 0.69	-126790.6 ± 2777.6
G026-012	224.25 ± 8.78	2068.89 ± 69.09	106.7 ± 10.22	0.968 ± 0.002	7.1 ± 0.62	-124144.6 ± 1593.2
G188-020	326.12 ± 16.9	6322.94 ± 761.96	231.5 ± 14.51	0.986 ± 0.003	32.68 ± 5.09	-74415.2 ± 4868.6
G188-030	357.1 ± 3.77	1217.92 ± 6.01	78.08 ± 0.76	0.915 ± 0.001	3.89 ± 0.04	-145163.2 ± 170.6

Table C1. Elemental abundances relative to Fe I ([X/Fe I]) determined using the model atmospheres given in Table 3 and EW measurements included online as supplementary material. The number of lines used for each measurement is given in brackets beside the abundance value. Conservative error estimates are adopted for each abundance measurement by choosing the largest of either the associated abundance error or variation in abundance due to the uncertainty in stellar parameters. Solar abundances are taken from (Asplund et al. 2009) and given below each element. Note that NLTE corrections are not included in this table but hfs corrections have been applied to the [Ba/Fe] abundances.

Abundance Solar Value	G037-037 ...	G158-100 ...	G184-007 ...	G189-050 ...	G233-026 ...	G262-021 ...
[Li/Fe]	1.40 ± 0.19 (1)
3.26 ± 0.05
[Na/Fe]	−0.10 ± 0.19 (2)	−0.83 ± 0.15 (1)	...	−0.54 ± 0.15 (1)	−0.45 ± 0.15 (1)	−0.20 ± 0.16 (2)
6.24 ± 0.03
[Mg/Fe]	0.06 ± 0.19 (1)	0.11 ± 0.15 (3)	−0.07 ± 0.20 (3)	−0.12 ± 0.20 (3)	0.38 ± 0.25 (2)	0.23 ± 0.16 (2)
7.60 ± 0.04
[Si/Fe]	0.42 ± 0.19 (1)	0.28 ± 0.15 (2)	0.09 ± 0.15 (3)	0.17 ± 0.16 (3)
7.51 ± 0.03
[Ca/Fe]	0.20 ± 0.06 (14)	0.18 ± 0.04 (17)	0.20 ± 0.07 (24)	0.17 ± 0.08 (27)	0.25 ± 0.04 (27)	0.34 ± 0.07 (23)
6.34 ± 0.04
[Sc II/Fe]	−0.09 ± 0.14 (1)	−0.10 ± 0.15 (2)	−0.04 ± 0.15 (2)	0.18 ± 0.16 (2)
3.15 ± 0.04
[Ti I/Fe]	0.30 ± 0.19 (3)	0.29 ± 0.06 (19)	0.23 ± 0.11 (32)	0.20 ± 0.13 (29)	0.27 ± 0.07 (15)	0.38 ± 0.11 (41)
4.95 ± 0.05
[Ti II/Fe]	0.37 ± 0.05 (7)	0.38 ± 0.04 (8)	0.34 ± 0.04 (11)	0.29 ± 0.04 (16)	0.20 ± 0.05 (12)	0.44 ± 0.05 (18)
...
[V/Fe]	0.30 ± 0.14 (2)	...	0.02 ± 0.15 (1)	0.30 ± 0.16 (3)
3.93 ± 0.08
[Cr I/Fe]	−0.14 ± 0.19 (2)	0.03 ± 0.06 (14)	0.15 ± 0.10 (17)	0.08 ± 0.13 (16)	0.04 ± 0.06 (11)	0.14 ± 0.11 (15)
5.64 ± 0.04
[Cr II/Fe]	0.18 ± 0.15 (3)	−0.28 ± 0.15 (2)	0.26 ± 0.16 (3)
...
[Mn/Fe]	...	−0.37 ± 0.15 (2)	−0.21 ± 0.14 (4)	−0.26 ± 0.15 (3)	−0.22 ± 0.15 (3)	−0.19 ± 0.16 (3)
5.43 ± 0.05
[Fe I/H]	−2.01 ± 0.08 (51)	−2.24 ± 0.05 (113)	−1.67 ± 0.07 (150)	−1.41 ± 0.10 (164)	−1.34 ± 0.06 (156)	−1.38 ± 0.07 (155)
7.50 ± 0.04
[Fe II/H]	−2.06 ± 0.04 (8)	−2.29 ± 0.03 (6)	−1.70 ± 0.05 (10)	−1.48 ± 0.05 (14)	−1.38 ± 0.04 (10)	−1.35 ± 0.06 (11)
...
[Co/Fe]	0.41 ± 0.15 (1)	0.13 ± 0.16 (1)
4.99 ± 0.07
[Ni/Fe]	−0.215 ± 0.19 (1)	0.06 ± 0.15 (4)	−0.07 ± 0.04 (17)	−0.11 ± 0.07 (18)	−0.08 ± 0.04 (19)	0.04 ± 0.04 (23)
6.22 ± 0.04
[Cu/Fe]	−0.44 ± 0.15 (1)	−0.15 ± 0.16 (1)
4.19 ± 0.04
[Zn/Fe]	0.09 ± 0.14 (2)	−0.15 ± 0.15 (2)	−0.12 ± 0.15 (2)	0.09 ± 0.16 (2)
4.56 ± 0.05
[Y II/Fe]	−0.11 ± 0.15 (1)	−0.02 ± 0.15 (1)	0.14 ± 0.16 (1)
2.21 ± 0.05
[Ba II/Fe]	0.25 ± 0.19 (2)	0.17 ± 0.15 (2)	0.13 ± 0.14 (4)	0.00 ± 0.15 (3)	0.08 ± 0.15 (3)	0.07 ± 0.16 (5)
2.18 ± 0.09
[α/Fe]	0.21 ± 0.10	0.23 ± 0.07	0.20 ± 0.14	0.17 ± 0.15	0.26 ± 0.05	0.36 ± 0.06